DOWNHOLE TEMPERATURE MODELING OF A HYDRAULICALLY FRACTURED

HORIZONTAL WELL USING PARALLEL COMPUTING


A Thesis

by

SHOHEI SAKAIDA



Submitted to the Office of Graduate and Professional Studies of
Texas A&M University
in partial fulfillment of the requirements for the degree of


MASTER OF SCIENCE



| | |
|---|---|
| Chair of Committee, | Alfred Daniel Hill |
| Committee Members, | Ding Zhu |
| | Debjyoti Banerjee |
| Head of Department, | Jeff Spath |



December 2019



Major Subject: Petroleum Engineering

ABSTRACT

Diagnosing hydraulic fracture performance is essential to evaluate and optimize fracturing treatment designs in horizontal wells. Distributed temperature sensing (DTS) is a valuable tool to monitor downhole conditions and diagnose hydraulic fractures. Although various temperature prediction models have been proposed to interpret the measured temperature data, quantitative interpretation is still challenging. To predict temperature in near-wellbore regions accurately, a forward model is needed to consider both reservoir and wellbore domains in transient conditions. In addition, the model has to be computationally efficient to implement history matching for field-scale reservoirs.

Yoshida et al. (2016) developed a comprehensive thermal and flow model and successfully interpreted the DTS temperature data. This numerical model consists of a reservoir model and a wellbore model, which are coupled iteratively through boundary conditions. In each domain, mass, momentum and energy conservation are solved in transient conditions to obtain profiles of wellbore and sandface temperature during fracturing treatment, shut-in, and production in a fractured well. This model enables us to interpret the DTS temperature quantitatively; however it is not practical for field applications from the point of view of computational efficiency.

This study presents a parallel version of the numerical thermal and flow model. Parallel computing is generally used as an effective way to improve computational speed. A parallel computing interface, MPI (Message Passing Interface) is implemented in this study because of its flexibility. The parallel model allows us to simulate the temperature in field-scale reservoirs

efficiently. Results of improvement are shown as comparisons of computational speed between

the original model and the parallel model during the processors of water injection and production.

CONTRIBUTORS AND FUNDING SOURCES

**Contributors**

**Funding Sources**

TABLE OF CONTENTS

LIST OF FIGURES

LIST OF TABLES

Page

CHAPTER 1

INTRODUCTION

1.1     Background and Literature Review

1.1.1   Downhole Temperature Measurements

To develop unconventional reservoirs, fracturing treatment design with narrower cluster spacing and more injection volume is common nowadays. This design generates complex fracture networks and requires a fracture diagnosis to further optimize the design. Interpreting downhole temperature is one of the diagnostic ways.

The downhole temperature has been used as a means to evaluate wellbore performance and downhole conditions since temperature logging was introduced by the development of accurate and rapid-resolving resistance thermometers in the 1930s (Hill 1990). Wellbore temperature initially dominated by the geothermal temperature is disturbed by fluid entries and unexpected fluid movement such as casing leaks and channels behind casing. Those temperature anomalies help to interpret the downhole conditions.

In addition to the temperature logging tool, distributed temperature sensing (DTS) technology using fiber-optic cables have become increasingly common to measure the downhole temperature recently. While the temperature logging tool measures a spatial temperature profile at a certain time, the DTS measurement provides temporally and spatially continuous temperature distribution permanently once it is installed. Monitoring the continuous temperature behavior allows for more accurate diagnosis of wellbore condition and performance. Also, the temperature logging tool is located only in a wellbore flow-path, but the fiber optic cable can be deployed not

only in the wellbore flow-path but also behind casing. Since the temperature in the flow-path very quickly becomes equal to the fluid temperature due to high flow rate during water injection, interpreting fluid distribution using the wellbore temperature can be challenging as suggested by Sierra et al. (2008). The deployment of fiber optic cable behind casing enables to interpret the downhole temperature from water injection through production periods without the direct influence by the fluid flowing in the wellbore.

Ugueto et al. (2015) showed the application of fiber optic distributed-sensing technology and qualitative interpretation of the DTS and distributed acoustic sensing (DAS) data. According to their plots, fracture locations and fluid distribution can be qualitatively identified by warm-back behavior in the temperature data. Also, they explain that effective zonal isolations can be indicated as the "stair-step" temperature profile.

## 1.1.2   Temperature Modeling for DTS Interpretation

To interpret the measured downhole temperature, various temperature prediction models have been proposed. Ramey (1962) presented an analytical method to predict the downhole temperature for single-phase flow with incompressible liquid or ideal gas in vertical injection and production wells. Since the geothermal temperature change is very small in horizontal wells, Yoshioka et al. (2005) developed a steady state wellbore temperature model coupled with a reservoir thermal model, which considered the subtle temperature behavior to interpret temperature in horizontal wells. They took Joule Thompson effect into account, which generates dominant marks to interpret gas production wells.

The downhole temperature has also been used to evaluate hydraulic fracturing treatments. Davis et al. (1997) presented a method to estimate fracture height using temperature logs after a

fracturing treatment in a vertical well. After the DTS temperature measurement was introduced for the diagnosis of fracturing treatment, some authors have proposed numerical thermal models to interpret temporally continuous temperature data quantitatively. Seth et al. (2010) presented a numerical thermal model coupled with fracture propagation model based on a simple volume balance to interpret the DTS temperature data during the fracturing treatment and shut-in period. Tabatabaei and Zhu (2012) implemented preliminary study to observe temperature behavior during water injection and warm-back period and the relation between fluid distribution and the downhole temperature using their numerical forward model and inversion method. Yoshida et al. (2014) showed the behavior of wellbore temperature and sandface temperature in a horizontal well with multiple hydraulic fractures by coupling a wellbore model and a reservoir model. Cui et al. (2015) applied their semi-analytical single-phase gas model for several field cases to quantitatively estimate inflow rate profiles by temperature history matching. A fully numerical flow and thermal two-phase model for a multi-stage fractured horizontal well was presented by Yoshida and Hill (2016). They also interpreted field DTS temperature data in one stage presented by Ugueto et al. (2015) and estimate fluid distribution using the developed forward model.

1.2     Research Objective

Although Yoshida et al. (2016) successfully interpreted the DTS data for the diagnosis of one stage, the fully numerical model is not computationally efficient. When the field data is interpreted, the field-scale fractured reservoir domain is discretized, and the temperature history matching needs to be implemented from water injection through production period. From the point of view of computational time, their numerical model is not practical to apply to the interpretation of field data. The objective of this research is to improve the computational efficiency of the

existing coupled reservoir and wellbore thermal model to interpret the field-scale DTS data efficiently. To accomplish it, a parallel computing method is introduced into the existing thermal model. It allows the model to deal with large number of grid blocks while maintaining accuracy of the computations.

CHAPTER 2

COUPLED RESERVOIR AND WELLBORE THERMAL MODEL

2.1     Model Description

Yoshida et al. (2016) developed the comprehensive thermal model to simulate downhole temperature in a hydraulically fractured horizontal well. His model is updated using the parallel computing in this work. This chapter provides governing equations and numerical solution method of the original model. Problems that the original model has are also clarified.

This comprehensive thermal model consists of a reservoir model and a wellbore model. Each domain solves distinct governing equations for fluid flow and energy transport numerically and obtains pressure, velocity, saturation/hold-up and temperature as solutions. Those two domains are solved under fully implicit scheme respectively and coupled iteratively.

2.1.1   Reservoir Model

The reservoir model is formulated for a three-dimensional reservoir domain in transient conditions with considerations of multiphase and multicomponent flow. It is divided into two governing equations such as fluid flow equation and thermal equation. The flow equation is described by mass balance equation of each component combined with Darcy's law.

*Flow Model*

According to Pruess et al. (1999), mass balance considerations in every subdomain into which the simulation domain is subdivided by the finite volume method describes that

$$\frac{d}{dt}\int_{V_n} M^i dV = \int_{\Gamma_n} \boldsymbol{F}^i \cdot \boldsymbol{n}\, d\Gamma + \int_{V_n} q^i dV, \quad i = w, g \tag{2.1}$$

where $V, V_n$ are volume and volume of subdomain $n$, $M^i$ is mass accumulation term of component $i$, $\Gamma_n$ is surface area of subdomain $n$, $\boldsymbol{F}^i$ is Darcy flux vector of component $i$, $\boldsymbol{n}$ is inward unit normal vector, $q^i$ is mass source/sink term of component $i$ and $t$ is time. The components can be water and gas $i = w, g$ in this model. The mass accumulation term, the flux term and the source/sink term in Eq. (2.1) are expressed as

$$M^i = \sum_{\beta=L,G} \phi S_\beta \rho_\beta X_\beta^i$$

$$\boldsymbol{F}^i = \sum_{\beta=L,G} \boldsymbol{F}_\beta^i \tag{2.2}$$

$$q^i = \sum_{\beta=L,G} X_\beta^i q_\beta$$

where $\phi$ is porosity, $\rho_\beta$ is density of phase $\beta$, $S_\beta$ is saturation of phase $\beta$, $X_\beta^i$ is mass fraction of component $i$ in phase $\beta$ and $q_\beta$ is phase-mass flow rate of phase $\beta$ per unit volume. The phase can be liquid and gaseous phase, $\beta = L, G$. Injection is positive in this model. The flux term, $\boldsymbol{F}_\beta^i$ is computed using Darcy's law.

$$\boldsymbol{F}_\beta^i = X_\beta^i \boldsymbol{F}_\beta$$

$$\boldsymbol{F}_\beta = -k\frac{k_{r\beta}\rho_\beta}{\mu_\beta}\left(\nabla P_\beta - \rho_\beta \boldsymbol{g}\right) \tag{2.3}$$

$$P_\beta = P_G + P_{c_{G\beta}}$$

$k$ is rock intrinsic permeability, $k_{r\beta}$ is relative permeability of phase $\beta$, $\mu_\beta$ is viscosity of phase

$\beta$, $P_\beta$ is pressure of phase $\beta$, $\mathbf{g}$ is gravitational acceleration vector and $P_{c_{G\beta}}$ is capillary pressure.

The capillary pressure is ignored to simplify problems in this work.

*Thermal Model*

In the same manner, the energy balance can be described as

$$\frac{d}{dt}\int_{V_n} M^\theta dV = \int_{\Gamma_n} \boldsymbol{F^\theta} \cdot \boldsymbol{n}\, d\tilde{A} + \int_{V_n} q^\theta dV \tag{2.4}$$

where $M^\theta$ is heat accumulation term, $\boldsymbol{F^\theta}$ is heat flux vector and $q^\theta$ is heat source/sink term.

The terms in Eq. (2.4) are

$$M^\theta = (1-\phi)\rho_R C_R T + \sum_\beta \phi S_\beta \rho_\beta U_\beta$$

$$\boldsymbol{F^\theta} = -k_\theta \nabla T + \sum_\beta H_\beta \boldsymbol{F_\beta} \tag{2.5}$$

$$q^\theta = q_{wb} + \sum_\beta H_\beta q_\beta$$

where $\rho_R$ is rock density, $C_R$ is heat capacity of the dry rock, $U_\beta$ is specific internal energy of phase

$\beta$, $k_\theta$ is composite thermal conductivity of the rock-fluid system, $H_\beta$ is specific enthalpy of phase

$\beta$, $T$ is temperature of fluid/matrix (thermal equilibrium), $q_{wb}$ is conductive heat transfer rate per

unit volume due to temperature difference.


2.1.2    Wellbore Model

The wellbore model is formulated for a one-dimensional domain in transient conditions

with considerations of multiphase and multicomponent flow. **Figure 2.1** shows a schematic

differential volume element in cylindrical coordinate system in this model. $v_z$ is z-directional

velocity to be solved, $I$ denotes that the properties are evaluated at inflow/outflow condition used only at the reservoir/wellbore contacts. Since the model is set as one-dimensional system, properties over the cross-sectional area are assumed constant of averaged properties in this work.
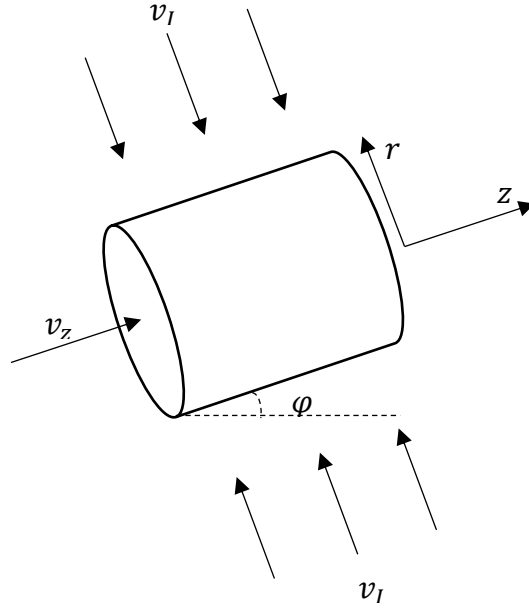


**Figure 2.1 Differential Volume Element of Wellbore Segment**

The wellbore model is also constructed by a flow model and a thermal model. The flow model is formulated by conservation of component mass with combined-phase momentum.

*Flow Model*

Assuming equilibrium of interphase mass transfer within a differential time, the conservation of component mass can be expressed as

$$\frac{\partial}{\partial t}\left(\sum_{\beta=L,G} y_\beta \rho_\beta X_\beta^i\right) + \frac{\partial}{\partial z}\left(\sum_{\beta=L,G} y_\beta \rho_\beta X_\beta^i v_{\beta,z}\right) = \frac{2\gamma}{r_i}\left(\sum_{\beta=L,G} y_{\beta,I}\rho_{\beta,I} X_{\beta,I}^i v_{\beta,I}\right) \qquad (2.6)$$

8

where $y_\beta$ is hold-up, $v_\beta$ is fluid in-situ velocity of phase $\beta$, $\gamma$ is pipe open ratio and $r_i$ is radius of well flow-path. The pipe open ratio defined by Yoshioka et al (2005) is used to consider the completion effects to inflow and outflow velocities.

$$\gamma = \frac{Open\ Pipe\ Surface\ Area}{Pipe\ Total\ Surface\ Area}$$

$$(0 \leq \gamma \leq 1)$$

(2.7)

$$v_I = \gamma v$$

(2.8)

The combined-phase momentum balance equation is computed as

$$\frac{\partial}{\partial t}\left(\sum_{\beta=L,G} y_\beta \rho_\beta\, v_{\beta,z}\right) + \frac{\partial P}{\partial z} + \frac{\partial}{\partial z}\left(\sum_{\beta=L,G} y_\beta \rho_\beta\, v_{\beta,z}^2\right) = -\frac{\Gamma}{2A}\rho v_m |v_m| f_m + \rho_m g_z$$

(2.9)

where $\Gamma$ is inner perimeter of the wellbore, $A$ is cross-sectional area of wellbore, $v_m$ is mean mixture velocity of center of mass and $f_m$ is phase-mixture friction factor on the wellbore wall. The mean mixture velocity $v_m$ is calculated by

$$v_m = \frac{\sum_\beta y_\beta \rho_\beta\, v_{\beta,z}}{\sum_\beta y_\beta \rho_\beta}$$

(2.10)

*Thermal Model*

The conservation of total energy in the wellbore can be expressed as

$$\frac{\partial}{\partial t}\left[\sum_{\beta=L,G} y_\beta \rho_\beta \left(U_\beta + \frac{v_\beta^2}{2}\right)\right]$$

$$= -\frac{\partial}{\partial z}\left[\sum_{\beta=L,G} y_\beta \rho_\beta \left(H_\beta + \frac{v_\beta^2}{2}\right)v_{\beta,z}\right] + \frac{\partial}{\partial z}\left(k_f \frac{\partial T}{\partial z}\right)$$

$$+ \sum_{\beta=L,G} y_\beta \rho_\beta \, g_{\beta,z} v_{\beta,z} + \frac{2(1-\gamma)}{r_i}(U_T)_{r=r_i}(T_{res} - T)$$

$$+ \frac{2\gamma}{r_i}\left[\sum_{\beta=L,G} j_{\beta,I} \rho_{\beta,I}\left(H_{\beta,I} + \frac{v_{\beta,I}^2}{2}\right)\right]$$

(2.11)

where $k_f$ is fluid thermal conductivity, $U_T$ is overall heat transfer coefficient, $j_{\beta,I}$ is volumetric flux of phase $\beta$ and $T_{res}$ is reservoir sandface temperature. The left-hand-side indicates the energy accumulation. In the right-hand-side, the first through third terms are advective energy flux, conductive energy flux and work done by body force, respectively. The rest of the terms are corresponding to the source/sink at the reservoir/wellbore contacts.

## 2.2    Constitutive Relations

In order to solve the governing equations, some dependent variables of the primary variables such as pressure, temperature, saturation/hold-up and velocity need to be computed. This section presents models to solve the dependent variables.

### 2.2.1    Key Parameters

*Relative Permeability*

Relative permeability is calculated by either linear model or Corey curve model (Corey, A.T. 1954) in this work. It is computed as a function of saturations shown below. The linear model is expressed as

$$k_{rL} = S_L$$
$$k_{rG} = S_G \tag{2.12}$$

where $k_r$ is relative permeability of $L$ (Liquid) and $G$ (Gaseous) phase. Since the pressure loss due to the flow in the hydraulic fractures can be ignored compared with one due to the flow of each fluid, the linear model is applied to compute the relative permeability in the fractures. On the other hand, the relative permeability in the formations is estimated by the following Corey curve model.

$$k_{rL} = \bar{S}^4$$
$$k_{rG} = (1 - \bar{S})^2 (1 - \bar{S}^2) \tag{2.13}$$

where $\bar{S}$ is the effective saturation which can be calculated by

$$\bar{S} = \frac{S_L - S_{rL}}{1 - S_{rL} - S_{rG}} \tag{2.14}$$

*Composite Thermal Conductivity*

The composite thermal conductivity is estimated by Somerton et al. (1974).

$$k_{Tt} = k_{dry} + \sqrt{S_L}(k_{wet} - k_{dry}) \tag{2.15}$$

where $k_{dry}$ is dry rock thermal conductivity (at $S_L = 0$) and $k_{wet}$ is water saturated rock thermal conductivity (at $S_L = 1$).

*Overall Heat Transfer Coefficient*

At the reservoir/wellbore contacts, the sandface temperature and wellbore temperature are solved by the energy balance equations including overall heat transfer coefficient. Geometric viewing of heat transfer in a wellbore is shown in **Figure 2.2**. The overall heat transfer coefficient for the possible cases are calculated by

Tubing Region;

$$\frac{1}{(U_T)_{r=r_{to}}} = r_{to} \left[ \frac{1}{r_{ti}h_t} + \frac{\ln\frac{r_{to}}{r_{ti}}}{k_t} + \frac{1}{r_{to}h_{ann}} + \frac{\ln\frac{r_{co}}{r_{ci}}}{k_c} + \frac{\ln\frac{r_w}{r_{co}}}{k_{cem}} \right] \qquad (2.16)$$

Casing/Perforated-Casing Regions;

$$\frac{1}{(U_T)_{r=r_{ci}}} = r_{ci} \left[ \frac{1}{r_{ci}h_c} + \frac{\ln\frac{r_{co}}{r_{ci}}}{k_c} + \frac{\ln\frac{r_w}{r_{co}}}{k_{cem}} \right] \qquad (2.17)$$

where $h$ is heat transfer coefficient, $k$ is thermal conductivity and $r$ is radius, and the subscripts $ti, to, ci, co, cem, w$ denote inner tubing, outer tubing, inner casing, outer casing, cement and wellbore, respectively.
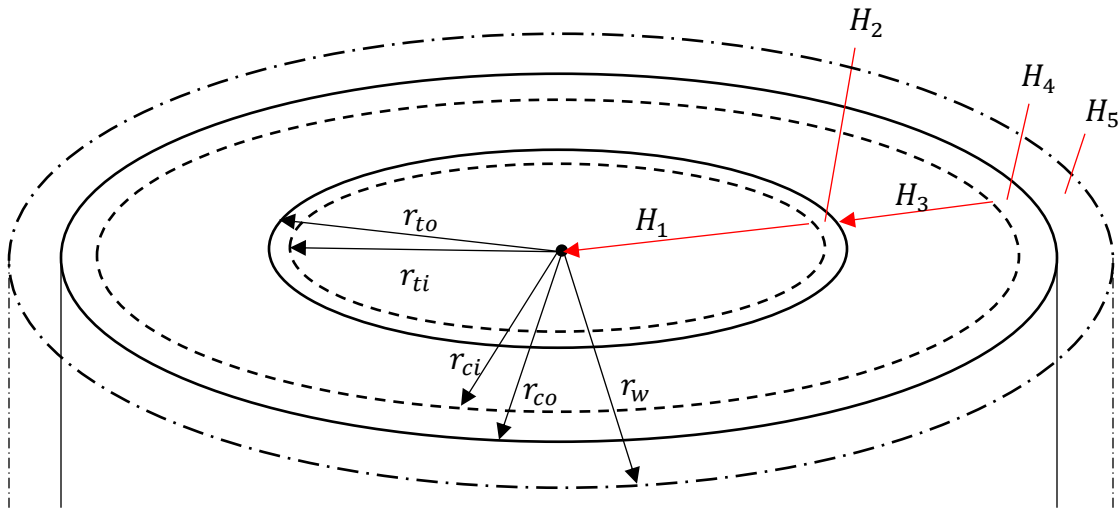


**Figure 2.2 Heat Transfer in Wellbore**

2.2.2    Phase Transition

This simulator is a two-phase flow model. Possible states are the following combinations such as "Liq" (Liquid), "Gas" (Gaseous) and "LqG" (Liquid and Gaseous). This section explains about the phase transition between the states.

12

*Mole Fraction and Partial Pressure*

Water and gas components can exist in both of the liquid and the gaseous phases. Component mole fraction $Y_\beta^i$ and mass fraction $X_\beta^i$ have the following constraints.

$$\sum_{i=w,g} X_\beta^i = 1$$
$$\sum_{i=w,g} Y_\beta^i = 1$$

(2.18)

In the gaseous phase, the component mixture is assumed to follow Dalton's law of partial pressures. The partial pressure of gas component is calculated by

$$p_G^g = Y_\beta^g p_G$$

(2.19)

where $p_G$ is gaseous phase pressure. For single-gaseous phase, the mole fraction of the gas component in the gaseous phase becomes one of the primary variables. Then, the partial pressure and mole fraction of the water component in the gaseous phase can be estimated.

On the other hand, if a liquid-gaseous two-phase system is considered, the partial pressure of the water component in the gaseous phase is equal to the saturation pressure $p_{sat}^w$. The mole fraction of the water component in the gaseous phase can be calculated by

$$Y_G^w = \frac{p_{sat}^w}{p_G}$$

(2.20)

The mole fraction of the gas component in the liquid phase is computed by Henry's law.

$$Y_A^g = \frac{p_G^g}{H^g}$$

(2.21)

where $H^g$ is the Henry's law coefficient.

For a single-liquid phase system, the mass fraction or mole fraction of the gas component in the liquid phase ($X_A^g$ or $Y_A^g$) becomes one of the primary variables.

*Phase Transition Criteria*

Phase transition criteria in multiphase multicomponent model are presented by Class et al. (2002). For the liquid-gaseous two-phase system, appearance and disappearance of the phases are determined by a value of the phase saturation. When the saturation of one phase becomes lower than zero, the state is switched to the single-phase condition such as either single-liquid or single-gaseous phase.

On the other hand, for the single-liquid phase system, the gaseous phase appears when the following criterion is satisfied.

$$p < p_{sat}^w + Y_A^g H^g \tag{2.22}$$

For single gaseous phase system, the criterion for the appearance of liquid phase is

$$p_{sat}^w < Y_G^w p_G \tag{2.23}$$

*Primary Variables*

Primary variables are determined by the phase system. **Figure 2.3** shows the schematic system of primary variables and phase transitions. The pressure and temperature are consistent primary variables for all of the three dynamic states such as single-liquid phase, single-gaseous phase and liquid-gaseous phase. Since the saturation is used only for the two-phase condition, mass or mole fraction is used as one of the primary variables to account for the solubility of the components in the single-phase condition. In the wellbore model, phase in-situ velocity $v_A$, $v_G$ or mixture velocity of the mass center $v_m$ is also one of the primary variables.

14
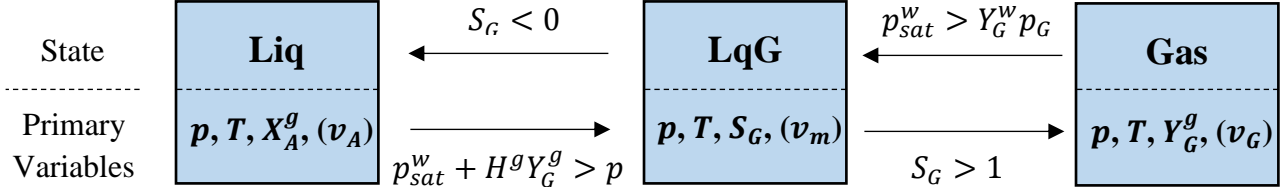
**Figure 2.3 Primary Variables and Phase Transition**

2.3     Implementation of Numerical Solution

This section describes implementation techniques to solve the above governing equations in this model. Those equations are discretized using the finite volume method and solved under fully-implicit scheme with the Newton-Raphson Method.

2.3.1     Numerical Solution Method

Both reservoir and wellbore domains are discretized by the finite volume method into conventionally small subdomains. The reservoir domain is discretized in the two-dimensional or three-dimensional spaces, and the wellbore domain is discretized into one-dimensional elements with defined connections. The zonal isolation between the fracturing treatment stages can be controlled by the connection conditions. The discretized final forms are shown below.

*Discretized Equations of Reservoir Model*

The governing equations Eq. (2.1) and Eq. (2.4) are discretized in spaces and time under fully-implicit scheme. Those are expressed using the residuals as

$$R_m^{i,n+1} = M_m^{i,n+1} - M_m^{i,n} - \frac{\Delta t}{V_m} \left( \sum_l A_{ml} F_{ml}^{n+1} + V_m q_m^{n+1} \right) = 0 \tag{2.24}$$

$$R_m^{\theta,n+1} = M_m^{\theta,n+1} - M_m^{\theta,n} - \frac{\Delta t}{V_m}\left(\sum_l A_{ml}F_{ml}^{\theta,n+1} + V_m q_m^{\theta,n+1}\right) = 0 \qquad (2.25)$$

where $n$ and $n+1$ are current and new timestep, $\Delta t$ is timestep size, $l$ is adjacent element of element $m$, $R^i$ is mass residual of component $i$, $R^\theta$ is energy residual and $A_{ml}$ is surface area between $m$ and $l$.

*Discretized Equations of Wellbore Model*

The governing equations Eq. (2.6), Eq. (2.9) and Eq. (2.11) are discretized in one-dimensional space and time. **Figure 2.4** shows schematic wellbore segments in this work. A staggered-grid system is used in the wellbore model to avoid spurious pressure oscillations. Since the velocities are solved at the faces of the segments, the center of control volume in the velocity field is set at the faces as shown in the figure. On the other hand, pressure and temperature are solved at the center of the segments. The subscript $m$ denotes the elements in the pressure and temperature field, and $k$ and $l$ denotes the element in the velocity field.
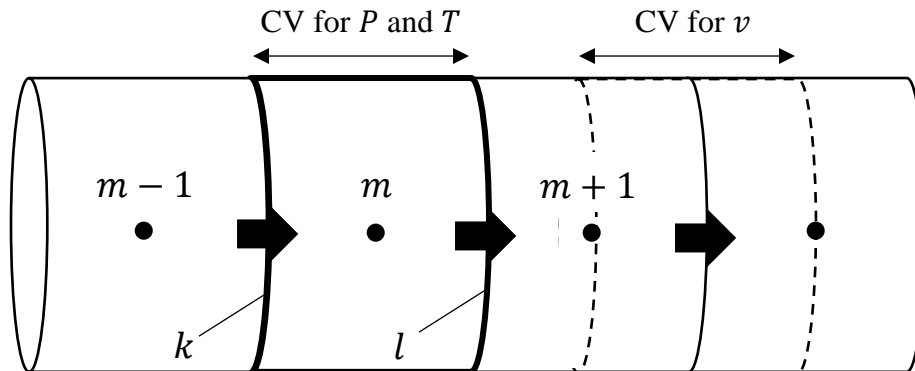


**Figure 2.4 Wellbore Control Volumes**

The equations of the component mass balance and the total energy are integrated over the control volume of the element $m$ in the pressure and temperature field. The final form of the residual equations are expressed as

$$
R_{v,m}^{n+1} = \sum_\beta y_{\beta,m}^{n+1} \rho_{\beta,m}^{n+1} X_{\beta,m}^{i,n+1} - \sum_\beta y_{\beta,m}^n \rho_{\beta,m}^n X_{\beta,m}^{i,n} + \frac{\Delta t}{V_m} \left( \sum_\beta X_{\beta,I}^{i,n+1} q_{\beta,I,m}^{n+1} \right)
$$

$$
- \frac{\Delta t}{V_m} \left( \sum_\beta A_k y_{\beta,k}^{n+1} X_{\beta,k}^{i,n+1} \rho_{\beta,k}^{n+1} v_{\beta,k}^{n+1} - \sum_\beta A_l y_{\beta,l}^{n+1} X_{\beta,l}^{i,n+1} \rho_{\beta,l}^{n+1} v_{\beta,l}^{n+1} \right)
$$

$$
= 0 \tag{2.26}
$$

where $q_{\beta,I,m}^{n+1}$ is mass inflow/outflow rate at the element $m$.

$$
R_{T,m}^{n+1} = \sum_\beta y_{\beta,m}^{n+1} \rho_{\beta,m}^{n+1} \left[ U_{\beta,m}^{n+1} + \frac{\left(v_{\beta,m}^{n+1}\right)^2}{2} \right] - \sum_\beta y_{\beta,m}^n \rho_{\beta,m}^n \left[ U_{\beta,m}^n + \frac{\left(v_{\beta,m}^n\right)^2}{2} \right]
$$

$$
- \frac{\Delta t}{V_m} \left[ A_k \left\{ \sum_\beta y_{\beta,k}^{n+1} \rho_{\beta,k}^{n+1} \left( H_{\beta,k}^{n+1} + \frac{\left(v_{\beta,k}^{n+1}\right)^2}{2} \right) v_{\beta,k}^{n+1} - \left( k_f \frac{\partial T}{\partial z} \right)_k^{n+1} \right\} \right.
$$

$$
\left. - A_l \left\{ \sum_\beta y_{\beta,l}^{n+1} \rho_{\beta,l}^{n+1} \left( H_{\beta,l}^{n+1} + \frac{\left(v_{\beta,l}^{n+1}\right)^2}{2} \right) v_{\beta,l}^{n+1} - \left( k_f \frac{\partial T}{\partial z} \right)_l^{n+1} \right\} \right] \tag{2.27}
$$

$$
- \Delta t \sum_\beta y_{\beta,m}^{n+1} \rho_{\beta,m}^{n+1} g_z v_{\beta,m}^{n+1} - \frac{\Delta t}{V_m} \left[ H_{\beta,I,m}^{n+1} + \frac{\left(v_{\beta,I,m}^{n+1}\right)^2}{2} \right]
$$

$$
- \Delta t \frac{2(1-\gamma)}{r_{i,m}} U_{T,m}^{n+1} \left( T_{res,m}^{n+1} - T_m^{n+1} \right) = 0
$$

The conservation of the combined-phase momentum is integrated over the velocity control volume of the element $k$. The final form of the residual equation is expressed as

$$R_{P,k}^{n+1} = \sum_{\beta} y_{\beta,k}^{n+1} \rho_{\beta,k}^{n+1} v_{\beta,k}^{n+1} - \sum_{\beta} y_{\beta,k}^{n} \rho_{\beta,k}^{n} v_{\beta,k}^{n} - \rho_{m,k}^{n+1} g_z \Delta t$$

$$+ \frac{\Gamma}{2A} \rho_{m,k}^{n+1} v_{m,k}^{n+1} |v_{m,k}^{n+1}| f_{m,k}^{n+1} \Delta t$$

$$+ \frac{\Delta t}{V_k} \left[ A_m \left( \sum_{\beta} y_{\beta,m}^{n+1} \rho_{\beta,m}^{n+1} v_{\beta,m}^{n+1} v_{\beta,m}^{n+1} \right) \right.$$

$$\left. - A_k \left( \sum_{\beta} y_{\beta,m-1}^{n+1} \rho_{\beta,m-1}^{n+1} v_{\beta,m-1}^{n+1} v_{\beta,m-1}^{n+1} \right) \right]$$

$$+ \frac{\Delta t}{V_k} (A_m p_m^{n+1} - A_{m-1} p_{m-1}^{n+1}) = 0$$

(2.28)

*Newton-Raphson Method*

The above residual equations in both domains are solved by the Newton-Raphson method. The concept of this method is that the residual equations are locally linearized by the Taylor series expansion using the current guess of the solutions. The primary variables are solved by

$$\delta x^{k+1} = -\mathbf{J}^{-1} \mathbf{R}$$
$$x^{k+1} = x^k + \delta x^{k+1}$$

(2.29)

where $k$ denotes current Newton-Raphson iteration, $\pmb{x}$ is vector of primary variables, $\pmb{\delta x}$ is update vector of primary variables, $\mathbf{J}$ is the Jacobian matrix and $\pmb{R}$ is the residual vector.

$$\pmb{J} = \begin{bmatrix} J_{11} & \cdots & J_{1j} & \cdots & J_{NN} \\ \vdots & \ddots & & \ddots & \vdots \\ J_{i1} & & J_{ij} & & J_{iN} \\ \vdots & \ddots & & \ddots & \vdots \\ J_{N1} & \cdots & J_{Nj} & \cdots & J_{NN} \end{bmatrix}$$

(2.30)

where the component of the Jacobian is

$$J_{ij} = \frac{\partial R_i}{\partial x_j}$$

(2.31)

18

where $R_i$ is the residual vector of the $i$-th element and $x_j$ is the primary variable vector of the $j$-th element. For each timestep, the Newton-Raphson iteration is repeated until convergence.

2.3.2    Coupling Procedure

At the reservoir/wellbore contacts, special treatments are needed to obtain the temperature at suitable locations for the DTS interpretation. This section describes the near wellbore treatment and the source/sink computations for both the reservoir and wellbore domains. Also, the coupling procedure in this work is explained.

*Near Wellbore Treatment*

Since the fiber-optic cable is installed behind casing, the sandface temperature which is the temperature at the reservoir/wellbore contacts needs to be obtained to interpret the DTS temperature. In order to compute the sandface temperature, the cylindrical coordinate grids are applied to the reservoir model near the wellbore regions using local grid refinement. When the local grids are used, the radial flow in a transverse fracture can also be considered. **Figure 2.5** shows a schematic of the radial flow in local cylindrical grids and the linear flow in Cartesian grids. The temperature in the adjacent reservoir grid block to the wellbore is computed as the sandface temperature. It is noted that the sandface temperature is not equal to the DTS temperature as shown in **Figure 2.6**.
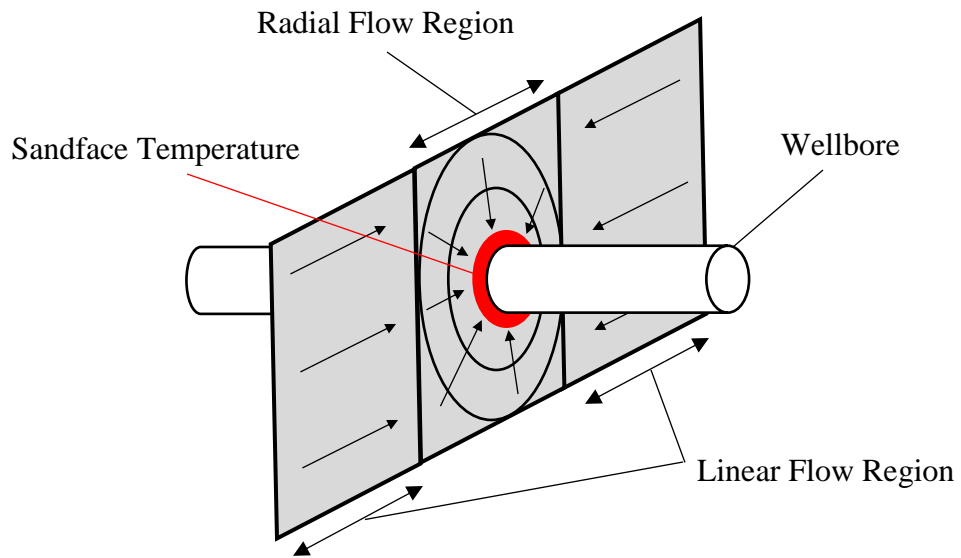
**Figure 2.5 Schematic of Local Grid Refinement**
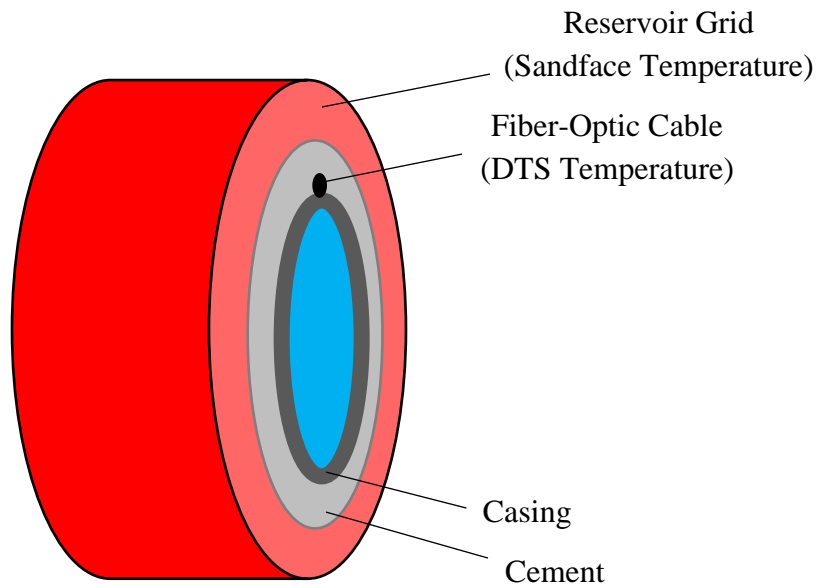


**Figure 2.6 Sandface Temperature vs DTS Temperature**

*Source/Sink Terms*

The reservoir model and wellbore model are coupled through the source/sink terms. The mass flow rate at the reservoir/wellbore contacts can be calculated by a productivity index concept presented by Coats (1977).

$$\dot{q}_\beta = \rho_\beta \lambda \, PI \left( p_{res} - p_{wf} \right) \tag{2.32}$$

where $\dot{q}_\beta$ is mass flow rate of phase $\beta$, $\lambda$ is mobility, $PI$ is the productivity index, $p_{res}$ is reservoir pressure and $p_{wf}$ is fluid pressure in the wellbore segment. The productivity index in cylindrical coordinate is calculated as the steady-state flow model.

$$PI = \frac{2\pi k_r \Delta x}{\ln \frac{r_{sand}}{r_w} + s} \tag{2.33}$$

where $k_r$ is permeability in the radial direction and $r_{sand}$ is the radial coordinate of the reservoir grid which contacts the wellbore grid.

On the other hand, the thermal source/sink terms are determined as the following heat transfer rate at the reservoir/wellbore contacts.

$$\dot{q}_{wb} = \frac{2(1-\gamma)}{r_i} (U_T)_{r=r_i} \left( T_{res} - T_{wf} \right) \tag{2.34}$$

where $\dot{q}_{wb}$ is heat transfer rate, $T_{res}$ is reservoir temperature and $T_{wf}$ is fluid temperature in the wellbore segment. The source/sink terms in both domains can be computed by the above equations.

*Solution Procedure*

The reservoir and wellbore model are solved separately under fully-implicit scheme and coupled iteratively. **Figure 2.7** shows the solution procedure for the coupled model.

Timestep $N$

**Wellbore Model**

Input $P_{res}$ and $T_{res}$
from Reservoir model

Compute Wellbore
Source/Sink ($\dot{q}_{\beta,w}, \dot{q}_{wb,w}$)

Newton-Raphson
Iterations

Solve Wellbore
Flow/Thermal Model

Obtain Wellbore
Primary Variables

**Reservoir Model**

Input $P_w$ and $T_w$
from Wellbore model

Compute Reservoir
Source/Sink ($\dot{q}_{\beta,res}, \dot{q}_{wb,res}$)

Newton-Raphson
Iterations

Solve Reservoir
Flow/Thermal Model

Obtain Reservoir
Primary Variables

No

$\left|\dot{q}_{\beta,w} - \dot{q}_{\beta,res}\right| \leq \epsilon_1$
and
$\left|\dot{q}_{wb,w} - \dot{q}_{wb,res}\right| \leq \epsilon_2$

Yes    $\epsilon_1, \epsilon_2$ : Convergence Criteria

Move to Timestep $N + 1$

**Figure 2.7 Workflow of Coupled Thermal Model**

In the wellbore model, the phase mass flow rate and the heat transfer rate are computed with the fixed reservoir properties, and the wellbore flow and thermal model are solved. This calculation is repeated in the Newton-Raphson iterations. Once the primary variables in the wellbore model are obtained, the reservoir model is solved with the fixed wellbore variables. Those computations are repeated until the changes of the phase mass flow rate and the heat transfer rate are sufficiently small or the maximum number of coupling steps assigned by a user is attained.

2.4     Analysis of Existing Model

To interpret the DTS temperature, the temperature history matching needs to be done by adjusting the fracture properties from the water injection to the production period. Therefore, the computational efficiency of forward model is a primary factor to interpret the temperature data efficiently, but the original model has a problem of computational. In this section, a solution approach to solve the problem is suggested.

2.4.1   Dominant Factors in Computational Time

By observing the computational behavior, possible factors influencing the computational time in this model can be listed as

- Large number of grid blocks

- High non-linearity in the wellbore model

*Fracture Treatment and Grid Number*

In this work, fractures are constructed as small grid blocks with fracture width and length, and the infinitely high permeability is assigned to the fracture regions to imitate an actual flow

behavior inside fractures. In addition, enhanced permeability zones are defined to control the leak off from the fractures. In order to mimic the fractures using thin grid blocks and to capture the diffusion of pressure and temperature around the fractures and wellbore accurately, the logarithmically incremented grid blocks are constructed as shown in **Figure 2.8**. Then, the total number of grid blocks becomes large even if the rough grids are used for far-away regions from the fracture. The number of grids directly influences the computational time.
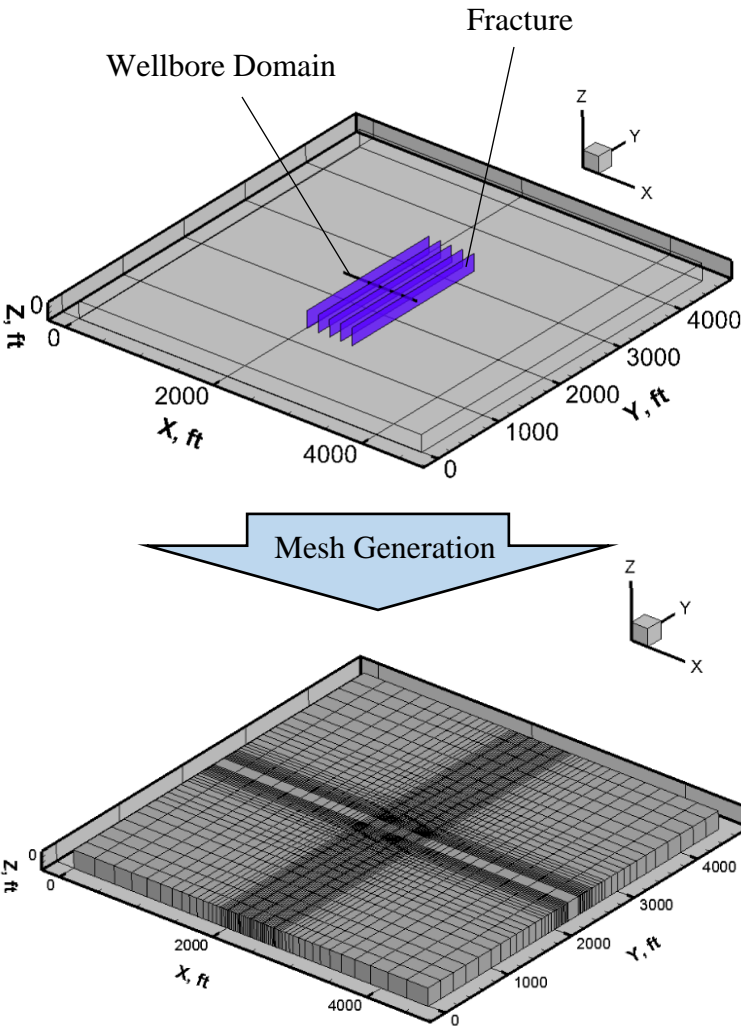
**Figure 2.8 Example of Mesh Generation (Five Fractures Case)**

24

*Non-linearity in Wellbore Model*

By the observation of computational behavior, slow convergence in the wellbore model makes the number of Newton-Raphson iterations larger, especially for simulations of the water injection period. The simulation of fluid flowing inside a small pipe with a high flow rate becomes a highly non-linear problem. It affects the stability of numerical model as well as the computational speed.

## 2.4.2 Motivation of This Work

While the stability of the wellbore model needs to be solved, it is not a direct solution to improve the computational efficiency. Also, the original model can solve the shut-in and production period stably. Therefore, parallel computing is suggested as the best approach to improve overall computational speed of the original model.

To monitor the computational time, an example case of water injection is simulated. A reservoir with five stages is set up using the number of grid blocks as shown in **Table 2.1**. The detailed input parameters are listed in **Table 5.1**. **Table 2.2** shows results of elapsed time for each computational section at a certain timestep. As shown in the results, this simulator needs the most computational time to construct the Jacobian matrix and to compute the primary and secondary variables for each element and connection in the reservoir model. It seems to be caused by element and connection loop operations for the large number of grid blocks. Since computations can be parallelized only in the same timestep, the routines of calculating the variables and the Jacobian matrix are parallelized. The detailed implementation of parallelization is explained in the next chapter.

**Table 2.1 Elapsed Time at a Certain Timestep**

|  | Wellbore Model | Reservoir Model |
|---|---|---|
| Number of Grids | 380 | 19056 |
| Elapsed Time for Jacobian Matrix Setup | 0.010 sec | 0.791 sec |
| Elapsed Time for Thermal & Physical Properties Computation | 0.014 sec | 2.001 sec |

CHAPTER 3

PARALLEL COMPUTING IMPLEMENTATION

3.1     Introduction to Message Passing Interface (MPI)

There are some approaches to parallelize the reservoir model. In this work, one of the most widely used parallel computing methods, Message Passing Interface (MPI) is used. This chapter describes a concept of MPI and how to apply it to the reservoir model.

A regular computer has two to four processor cores and four to eight threads on each processor. **Figure 3.1** shows the computer which has two processor cores and four threads as an example. The definitions of processor and thread are an executing instance of program and a subset of the processor, respectively. In general, computations are executed using a single processor and a single thread as shown in **Figure 3.2**. The basic idea of parallel computing is to divide the overall computation and let each processor or thread execute the portion of the computation. MPI is a standardized means of distributing data using multiple processors while another parallel computing method, OpenMP divides computations using multiple threads. Since super computer has much more processors than regular computers, running MPI parallel model on super computer is expected to improve computational efficiency.

*Simple Reservoir Simulation; Parallel Element Loop*

For instance, a simple isothermal reservoir simulation described as the residual form in the following equation is run to obtain the pressure profile over $8 \times 4 \times 1$ grid blocks.

$$R_i^{n+1} = M_i^{n+1} - M_i^n - \frac{\Delta t}{V_i}\left(\sum A_j F_j^{n+1} + V_i q_i^{n+1}\right) = 0 \tag{3.1}$$

27

In general, the accumulation terms, $M_i$ on all of the elements are simply computed by 32 times element loop. Parallel computing allows us to divide the 32 grid blocks into some portions, for example 8 grids × 4 subdivisions, and to compute the variables in each subdivision simultaneously as shown in **Figure 3.3 (a)**. In other words, the variables on each subdivision are calculated using a local element loop in each processor as shown in **Figure 3.3 (b)**.
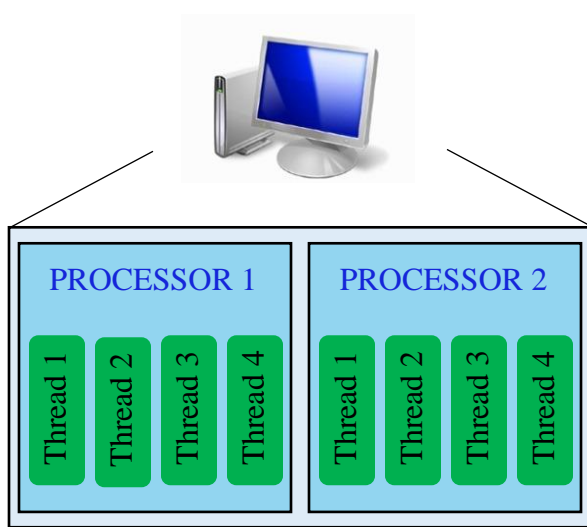


**Figure 3.1 Schematic of 2 Processors & 4 Threads**
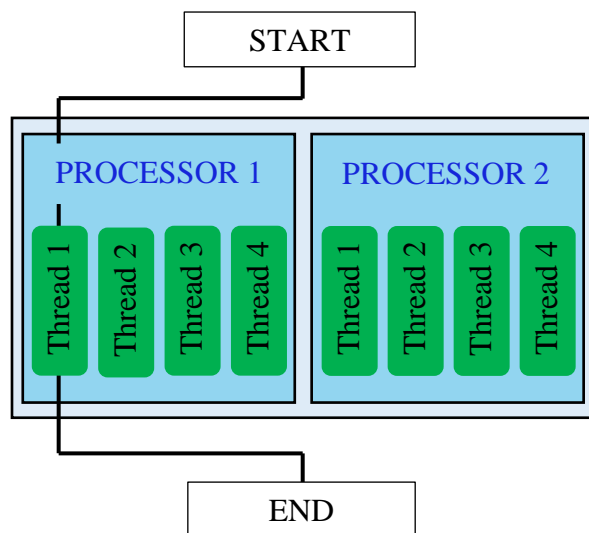


**Figure 3.2 Single Computation Process**

Element-Based Variables

Element-Based Variables

8 × 4 × 1 Grid Blocks

8 Grids × 4 Subdivisions

**(a) Divided Reservoir Domain**

Start Element Loop

$i$: Element #

| PROCESSOR 1 | PROCESSOR 2 | PROCESSOR 3 | PROCESSOR 4 |
|---|---|---|---|
| $i = 1 \sim 8$ | $i = 9 \sim 16$ | $i = 17 \sim 24$ | $i = 25 \sim 32$ |

END
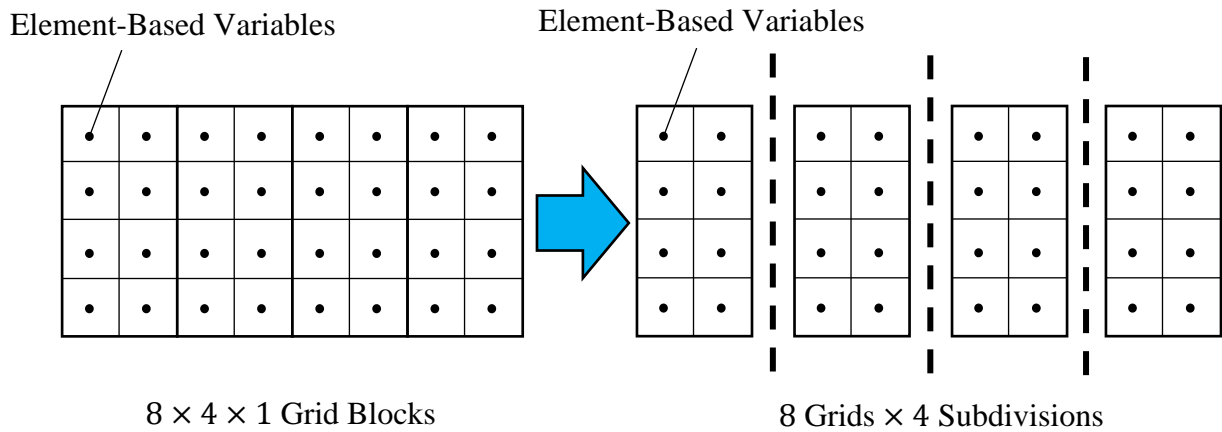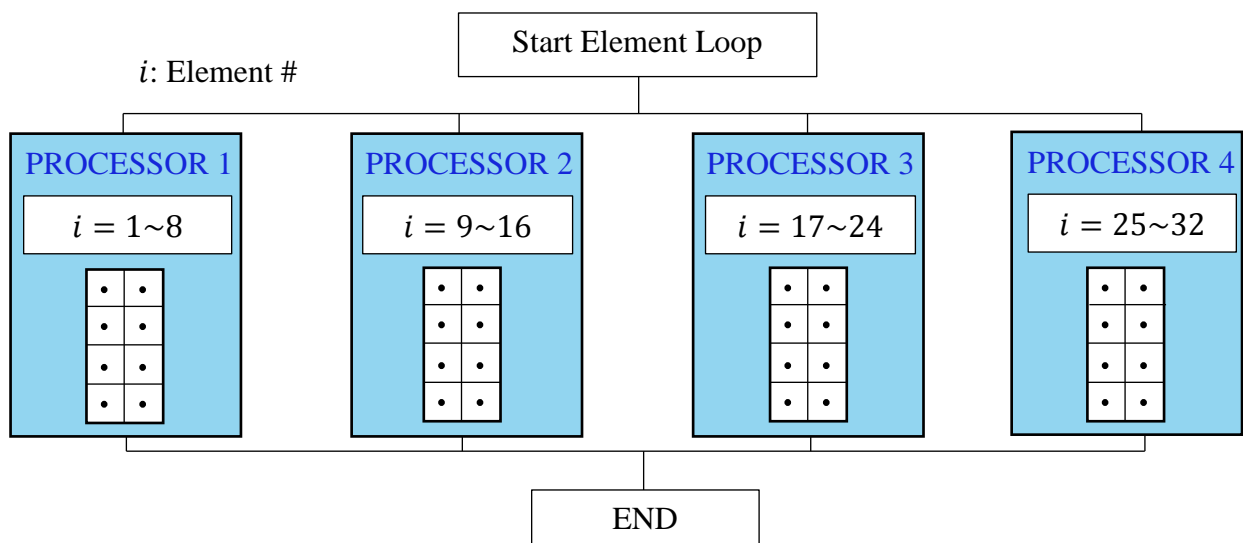
**(b) Parallel Computing Procedure Using 4 Processors**

**Figure 3.3 Parallel Element Loop**

*Simple Reservoir Simulation; Parallel Connection Loop*

An issue of implementing parallel computing is how we compute the flux term, $F_j^{n+1}$ which is estimated at the face between the element $i$ and the vicinities. Since the computations in each processor are independent, the divided connections by two processors need a special treatment to compute the flux term there. The issue is solved by data communication routines in MPI. MPI has the function for sending and receiving data between processors. For example, if the data stored in the processor 2 is required to compute the flux term in the processor 1, the data can be sent from the processor 2 to the processor 1. The simplest way to implement the data communications is to store the sent data from other processors in dummy elements before a connection loop starts as shown in **Figure 3.4** and **Figure 3.5 (a)**. The dashed line-grids represent the dummy elements. Also, the connection loop computations are explained schematically in **Figure 3.5 (b)**.
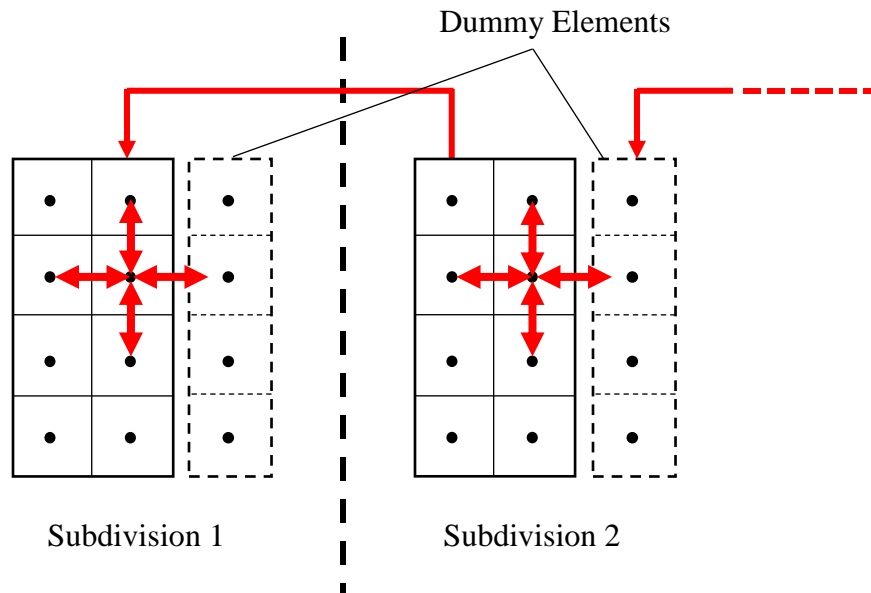


**Figure 3.4 Concept of Dummy Elements**

Connection-Based Variables

Connection-Based Variables

$8 \times 4 \times 1$ Grid Blocks

8 Grids × 4 Subdivisions

**(a) Divided Reservoir Domain**

**Set Up Dummy Elements (Data Communications)**

Start Connection Loop

$j$: Connection #

| PROCESSOR 1 | PROCESSOR 2 | PROCESSOR 3 | PROCESSOR 4 |
|---|---|---|---|
| $j = 1{\sim}14$ | $j = 15{\sim}28$ | $j = 29{\sim}42$ | $j = 43{\sim}52$ |

END
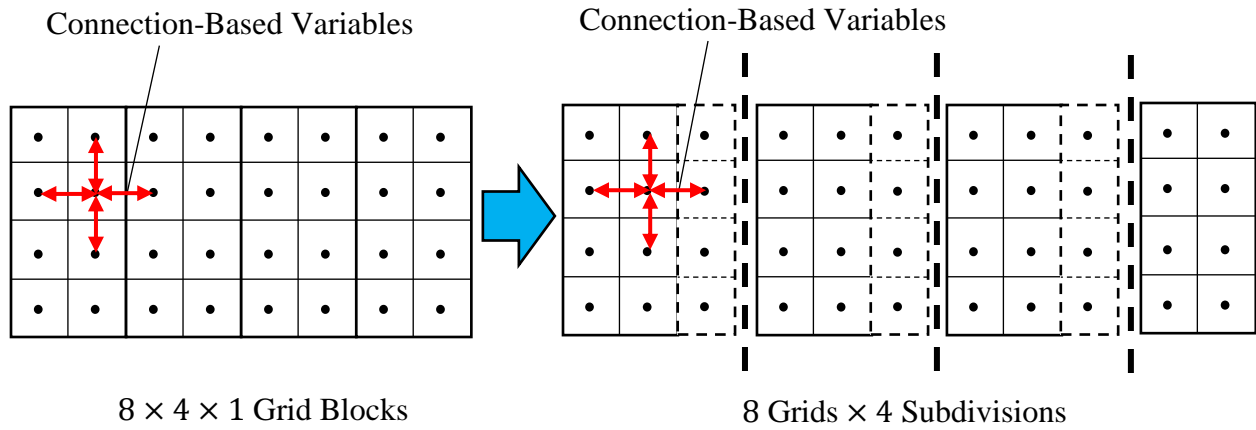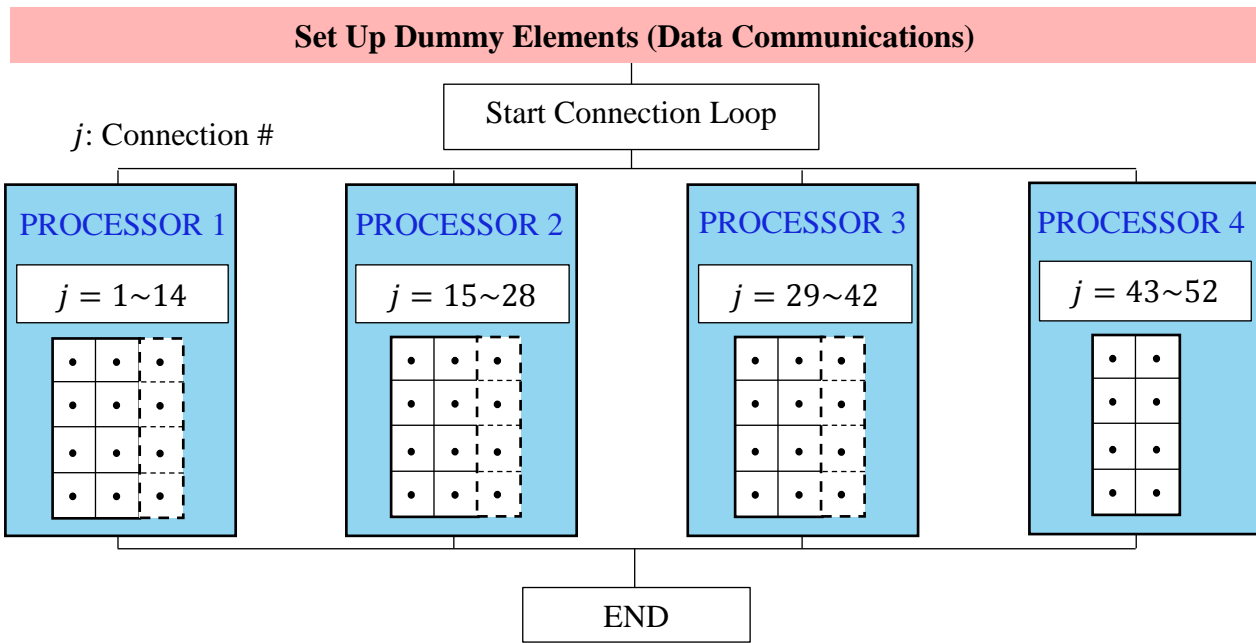
**(b) Parallel Computing Procedure Using 4 Processors**

**Figure 3.5 Parallel Connection Loop**

3.2     Parallel Reservoir Model

Because the wellbore domain is solved as one-dimensional model, it is a much smaller problem computationally compared with the reservoir model. The computational time in each time step is short enough as shown in **Table 2.2**. Therefore, only the reservoir model is parallelized in this work. The wellbore model is simulated in a certain main processor, and the solutions are distributed to the other processors as the source and sink terms. The workflow of the coupled wellbore and parallel reservoir model is shown in **Figure 3.6**. The routines written in red are parallelized.
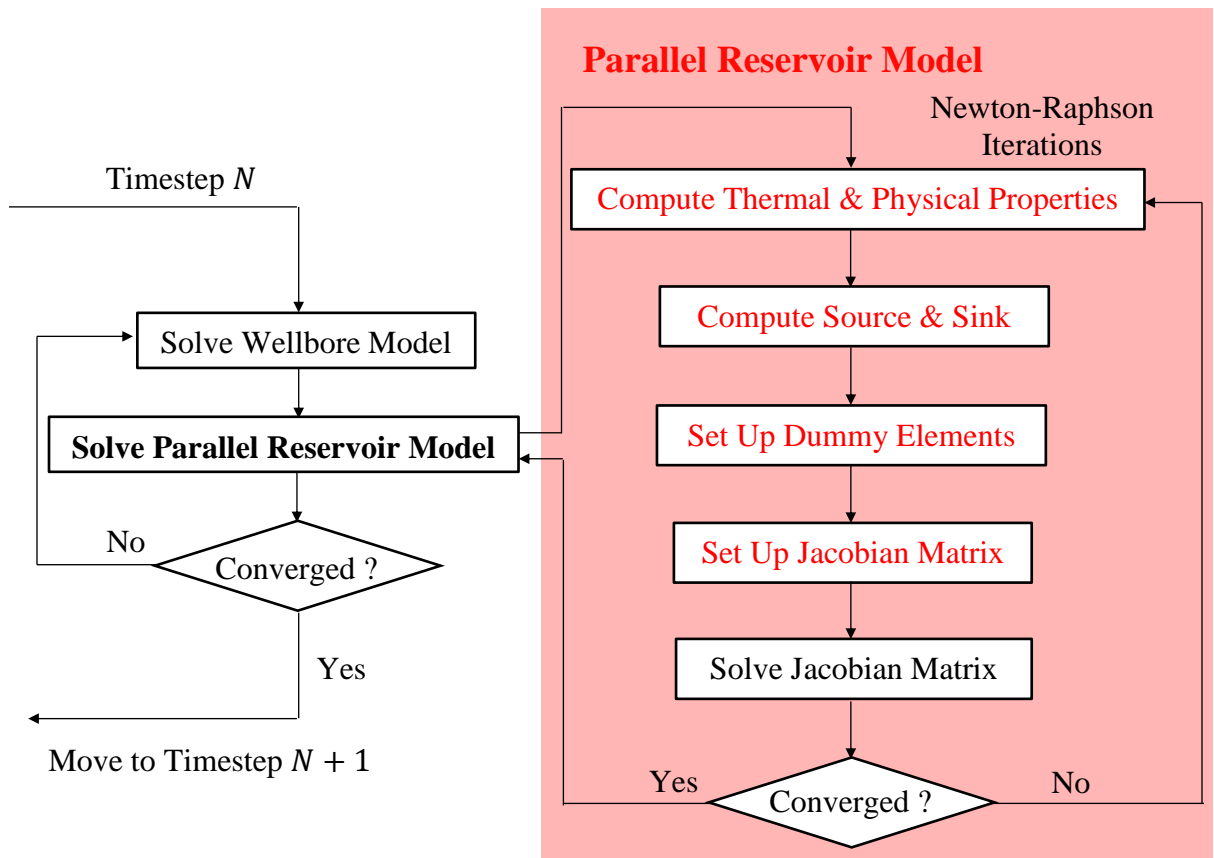


**Figure 3.6 Workflow of Coupled Wellbore and Parallel Reservoir Model**

**Figure 3.7** explains the procedure of the parallel reservoir model using four processors schematically. The procedure is similar to the example of the simple isothermal reservoir simulation. To calculate Eq. (2.25) and Eq. (2.26), the thermal and physical properties are estimated based on the primary variables at each iteration of the Newton-Raphson method. Since those properties are computed only in the element loop, we can simply parallelize the element loop without the data communication. If there are source and sink elements in the processor, those are computed only in the processor.

Then, the computed thermal and physical properties are stored in the dummy elements by using the data communications. The local Jacobian matrices are calculated in each processor. Finally, a global Jacobian matrix is constructed by combining the local ones and solved in the main processor. Those routines are repeated until the convergence is confirmed in the main processor.

Start Parallel Reservoir Model

PROCESSOR 1 | PROCESSOR 2 | PROCESSOR 3 | PROCESSOR 4

**Computation of Thermal and Physical Properties**

**Element Loop** $i = 1, n_1$

**Element Loop** $i = n_1 + 1, n_2$

**Element Loop** $i = n_2 + 1, n_3$

**Element Loop** $i = n_3 + 1, N$

$\phi_i(P,T)$
$k_{r,i}(S)$
$\rho_i(P,T)$
$\mu_i(P,T)$
$\vdots$

$\phi_i(P,T)$
$k_{r,i}(S)$
$\rho_i(P,T)$
$\mu_i(P,T)$
$\vdots$

$\phi_i(P,T)$
$k_{r,i}(S)$
$\rho_i(P,T)$
$\mu_i(P,T)$
$\vdots$

$\phi_i(P,T)$
$k_{r,i}(S)$
$\rho_i(P,T)$
$\mu_i(P,T)$
$\vdots$

**Compute Source and Sink Term**

**Set Up Dummy Elements (Data Communications)**

**Set Up Jacobian Matrix**

**Element Loop** $i = 1, n_1$

**Element Loop** $i = n_1 + 1, n_2$

**Element Loop** $i = n_2 + 1, n_3$

**Element Loop** $i = n_3 + 1, N$

Accumulation Term $M_i, M_i^\theta$

Accumulation Term $M_i, M_i^\theta$

Accumulation Term $M_i, M_i^\theta$

Accumulation Term $M_i, M_i^\theta$

**Connection Loop** $j = 1, nc_1$

**Connection Loop** $j = nc_1 + 1, nc_2$

**Connection Loop** $j = nc_2 + 1, nc_3$

**Connection Loop** $j = nc_3 + 1, N_c$

Flux Term $F_j, F_j^\theta$

Flux Term $F_j, F_j^\theta$

Flux Term $F_j, F_j^\theta$

Flux Term $F_j, F_j^\theta$

Combine Local Jacobian Matrices

Solve Jacobian Matrix

End Parallel Reservoir Model

$i$: Element #
$N$: Total Element #

$j$: Connection #
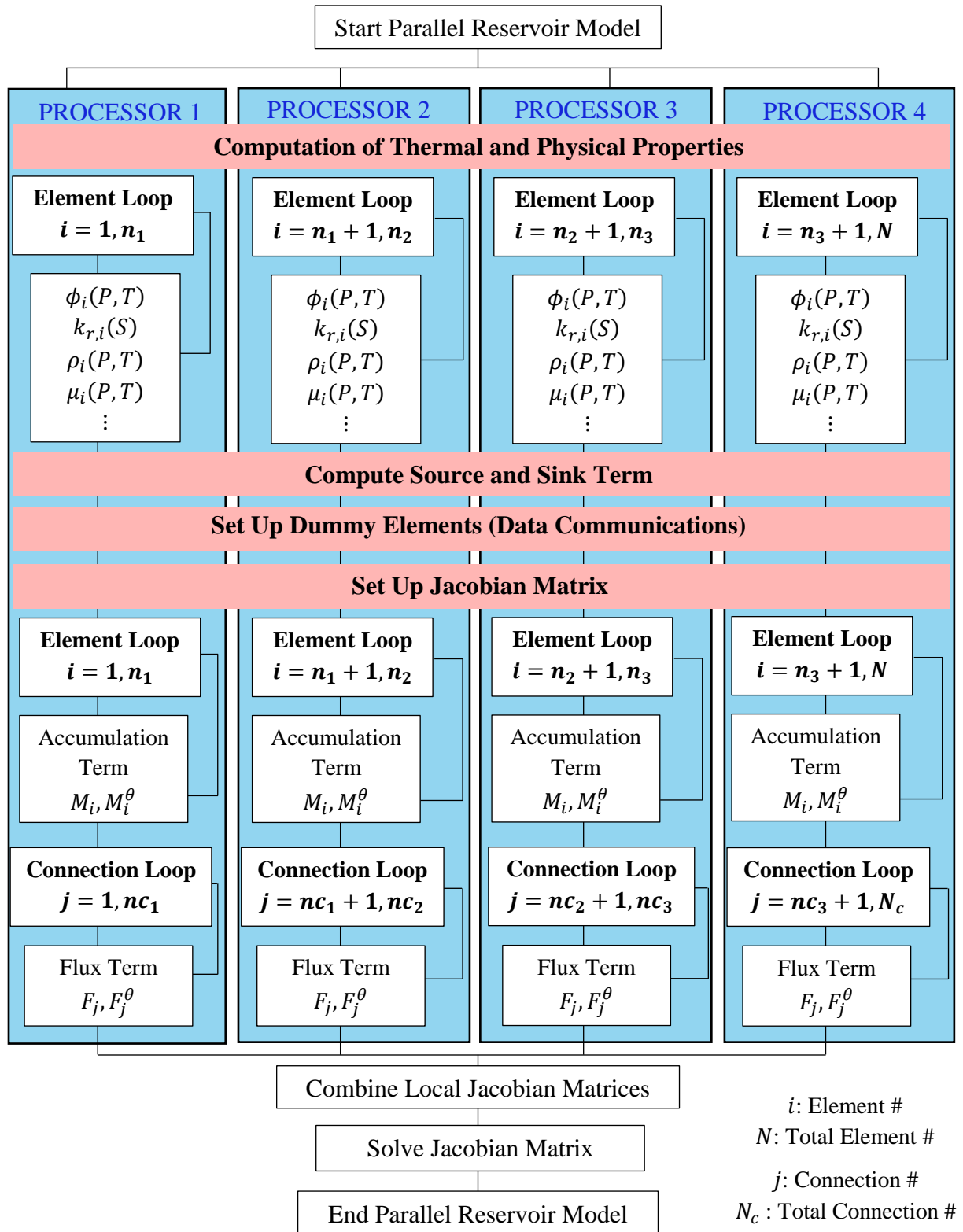$N_c$ : Total Connection #

**Figure 3.7 Computational Procedure of Parallel Reservoir Model**

34

CHAPTER 4

VERIFICATION OF PARALLEL MODEL

4.1    Case of Horizontal Well with Single Fracture

In this chapter, the parallel model is verified against the original model. Some case studies

Yoshida (2016) implemented are used for the verification. A horizontal well with a single fracture

is set up as the first case. To follow the real fracturing treatment procedure, water injection, shut-

in and production stages are simulated continuously. In this work, a gas-water two-phase system

is considered. For simplicity, the heat transfer between the reservoir and the wellbore is ignored in

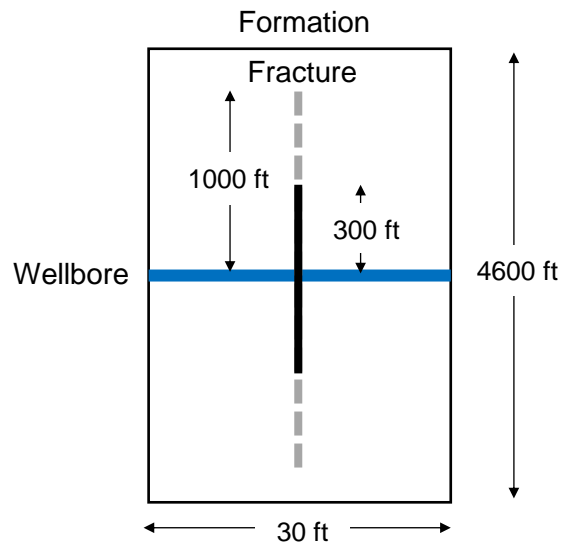this case. **Figure 4.1** shows the geometry of the domain to be solved.



**Figure 4.1 Model Setup for Single Fracture Case**

**Table 4.1 Main Input Parameters for Single Fracture Case**

| Reservoir Properties | |
|---|---|
| Length, ft | 30 |
| Width, ft | 4600 |
| Thickness, ft | 160 |
| Matrix Permeability, mD | 5.83E-04 |
| Matrix Porosity | 0.042 |
| Total Thermal Conductivity, Btu/(ft-hr-°F) | 0.924 |
| Rock Specific Heat, Btu/(lbm-°F) | 0.202 |
| Rock Density, lbm/ft3 | 148.58 |
| Initial Water Saturation | 0.1 |
| Initial Pressure, psi | 4500 |
| Initial Temperature, °F | 238.37 |

| Fracture Properties | |
|---|---|
| Fracture Width, in | 0.24 |
| Fracture Height, ft | 160 |
| Fracture Half-Length (Injection), ft | 1000 |
| Fracture Half-Length (After Shut-in), ft | 300 |
| Fracture Conductivity (Injection), D-ft | 10 |
| Fracture Conductivity (After Shut-in), D-ft | 0.02 |
| Fracture Porosity | 0.2 |
| Enhanced Permeability, mD | 5.83E-03 |

| Treatment Information | |
|---|---|
| Injection Time, min | 100 |
| Injection rate, bpm | 18 |
| Injection Fluid Temperature, °F | 80 |

**Table 4.1** shows the main input parameters for this verification study. The fracture length is set as

1000 ft during the injection period. After the shut-in, the fracture length is reset as 300 ft to mimic

the fracture closure.

4.1.1    Water Injection

In the numerical simulation, the fracture is assumed to be created immediately at the

beginning of injection because the fracture propagation is not considered in this model. The fluid

36

flowing inside fracture is considered using the high rock permeability and the relative permeability computed by the linear model in the fracture grid blocks. The boundary condition at the reservoir edges is given as no-flow boundary. **Figure 4.2** shows the verification result of temperature profile and water saturation along the fracture, respectively.

4.1.2   Shut-in

Using the obtained pressure, temperature and saturation distribution as initial conditions, 30 days of shut-in in the same domain is simulated. The reservoir region around the fracture cooled down by the injection fluid is heated up by the geothermal heating during the warm-back period. **Figure 4.3** shows the verification result of warm-back temperature along the fracture. Although it depends on the shut-in period, the reservoir temperature does not recover to the original geothermal temperature completely at the end of shut-in in this case.
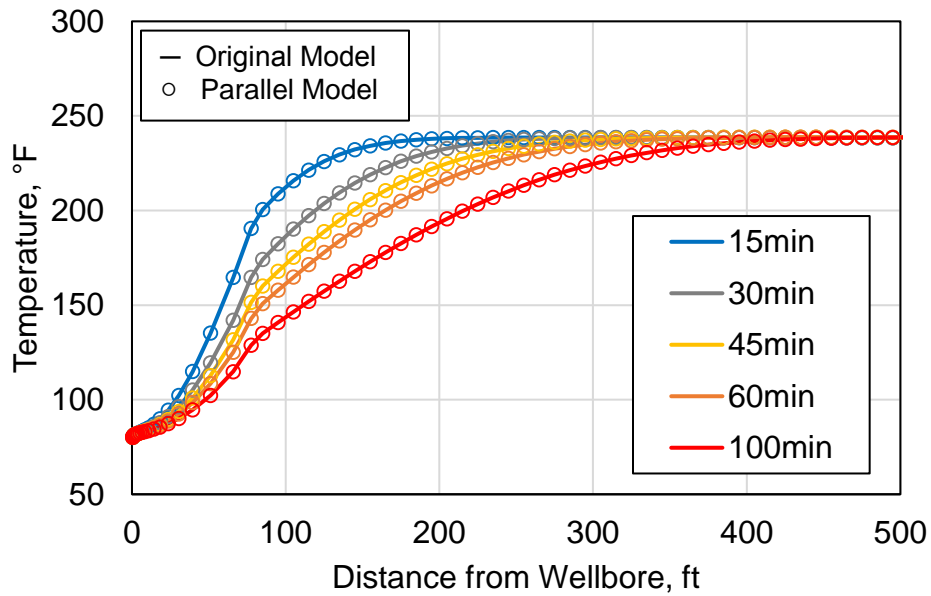
(a) Verification of Temperature
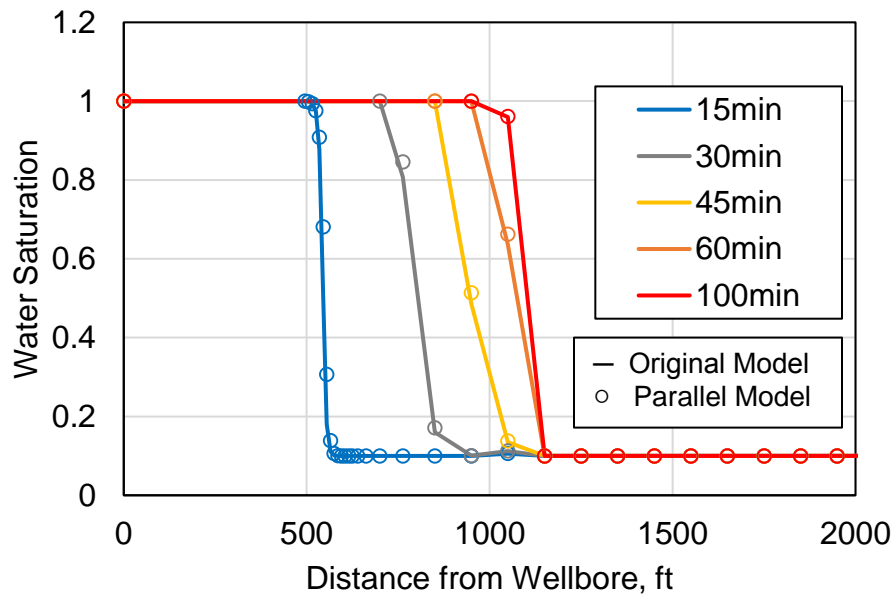


(b) Verification of Saturation

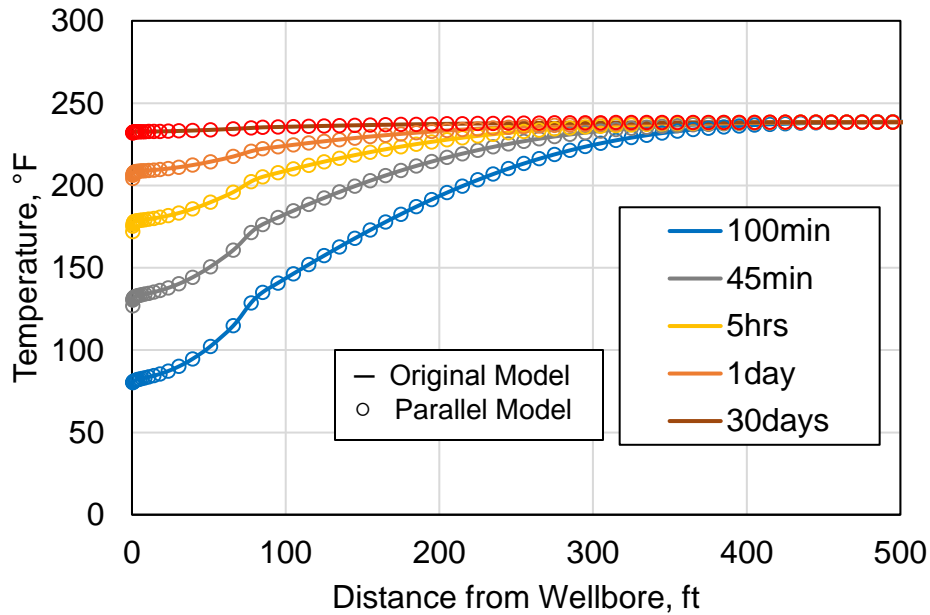**Figure 4.2 Verification of Water Injection Case**

**Figure 4.3 Verification of Shut-in Case**

### 4.1.3 Production

After the injection and shut-in, 100 days of production is simulated using the distribution of primary variables obtained in the previous simulation for shut-in as initial conditions. **Figure 4.4** shows the water and gas production rate. Only water is produced until 0.1 day of production. After that, the gas production becomes dominant. **Figure 4.5** shows the relationship between the production rate and the inflow temperature which is the sandface temperature at the fractured location. The temperature decreases as the gas production increases due to Joule-Thompson cooling effect.

According those results, the parallel model is verified that it obtains the primary variables in both the reservoir and wellbore domains during the water injection, shut-in and production period in the same way as the original model does.
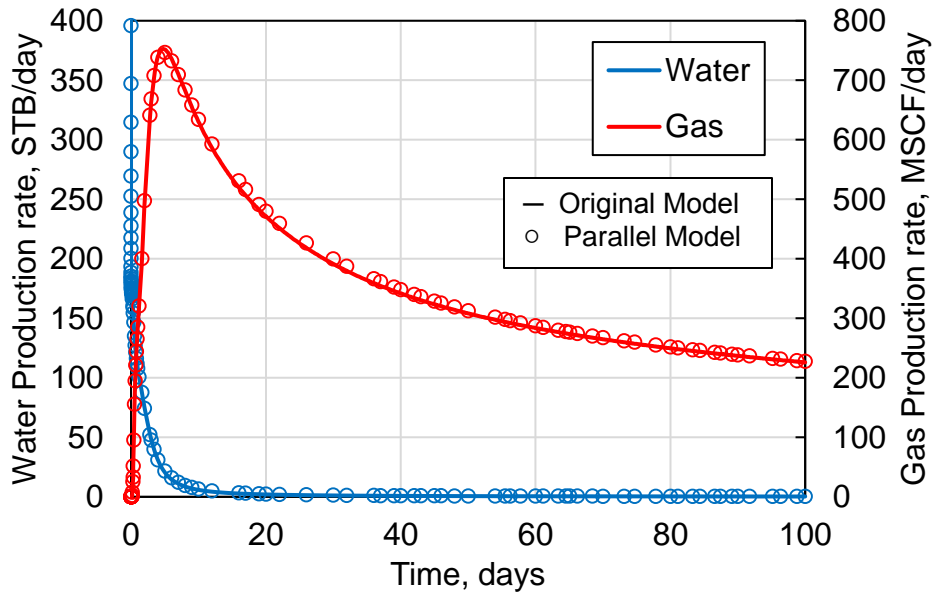
(a) Verification of Production rate
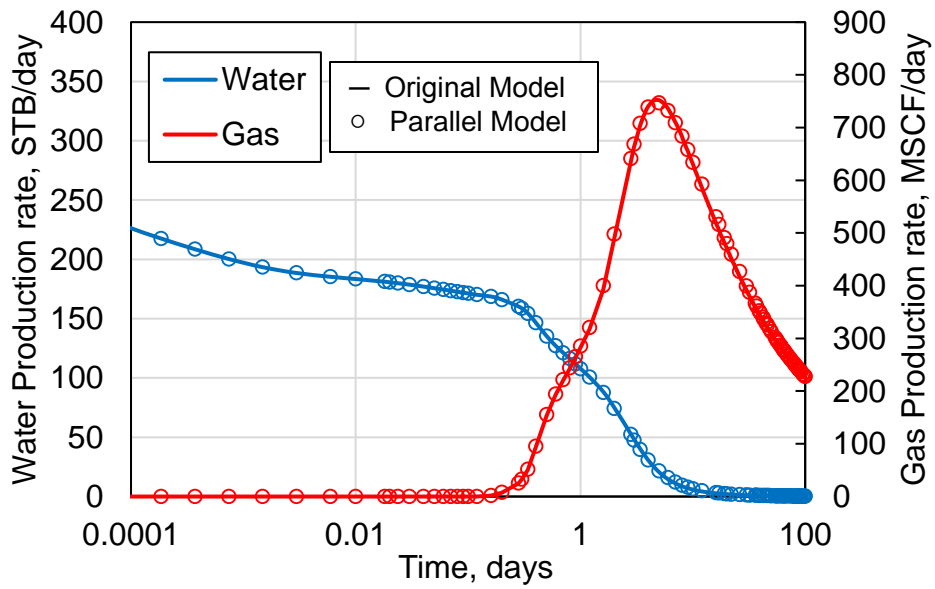


(b) Verification of Production rate (Semi-log)

**Figure 4.4 Verification of Production rate**
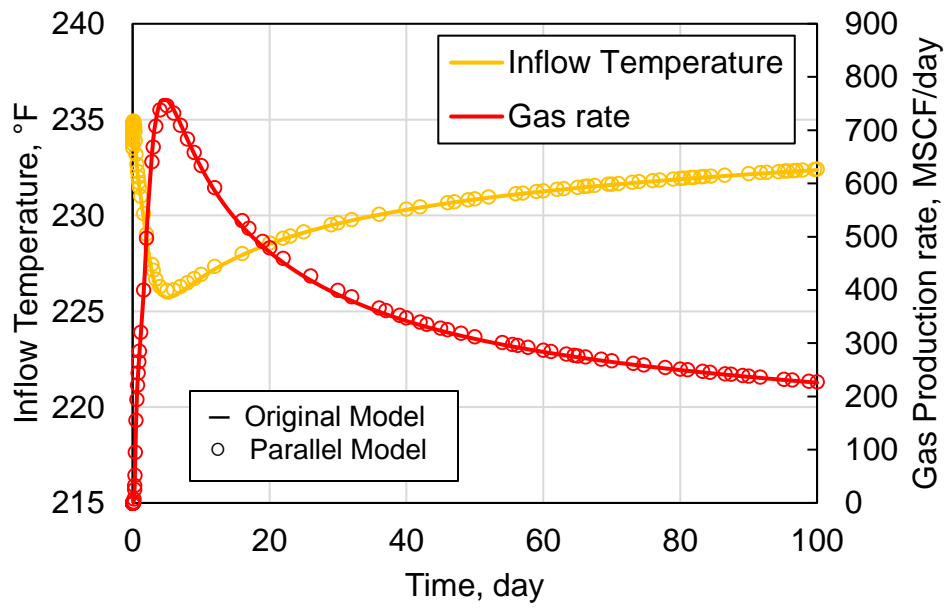
(a) Verification of Inflow Temperature
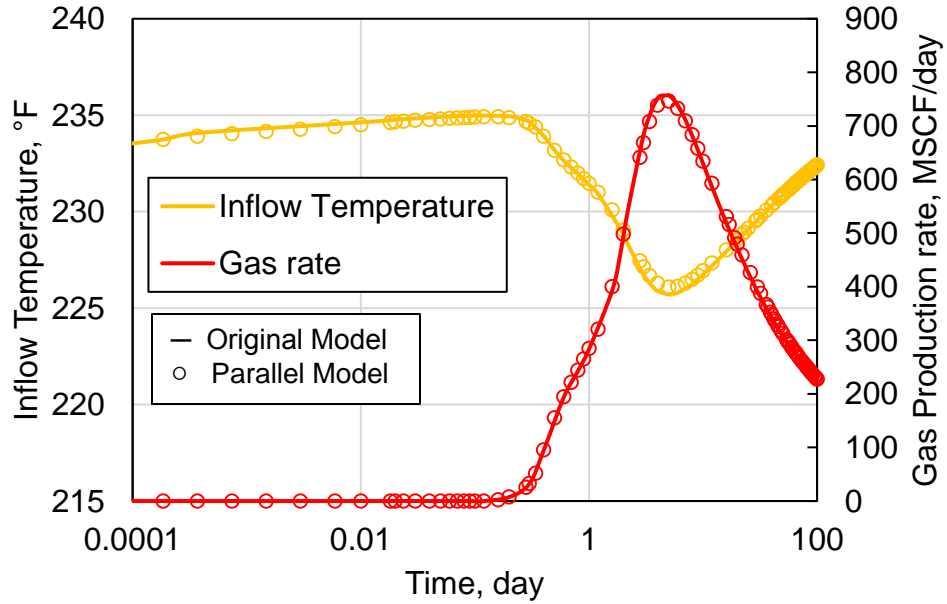


(b) Verification of Inflow Temperature (Semi-Log)

**Figure 4.5 Verification of Inflow Temperature**

41

## 4.2 Case of Horizontal Well with Multiple Fractures

Next, the treatment of a single stage which has five identical fractures in a horizontal well is simulated. This reservoir is also considered as a gas-water two-phase system. In this section, the computations of wellbore temperature and heat transfer between the reservoir and the wellbore are verified. **Figure 4.6** shows the geometric information of the domain to be solved. **Table 4.2** shows the main input parameters used in this case. This case also simulates from the injection to production period. In the simulation of multiple fractures, water is injected from the heel side and evenly distributed to each fracture using the prescribed flow rate in this identical fractures case.



**Figure 4.6 Model Setup for Identical Five Fractures Case**

**Table 4.2 Main Input Parameters for Five Fractures Case**

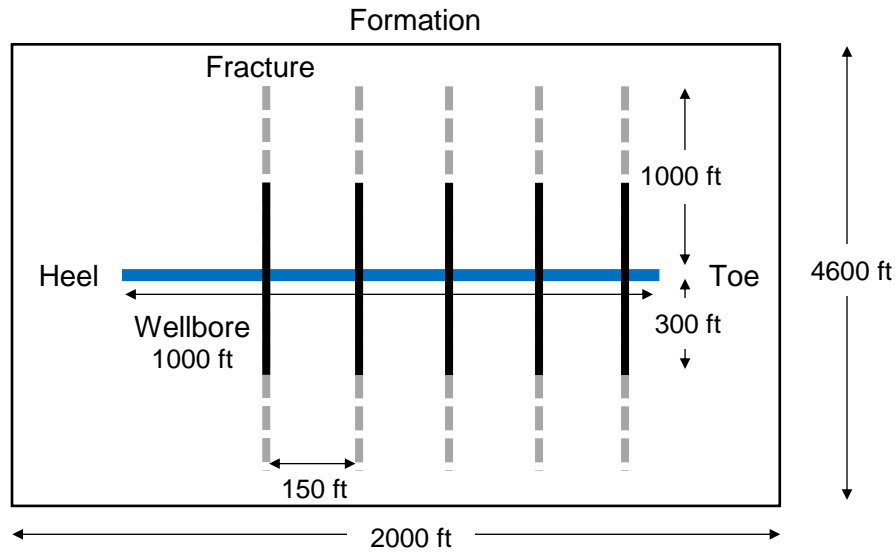| Reservoir Properties | |
|---|---|
| Length, ft | 2000 |
| Width, ft | 4600 |
| Thickness, ft | 160 |
| Matrix Permeability, mD | 5.83E-04 |
| Matrix Porosity | 0.042 |
| Total Thermal Conductivity, Btu/(ft-hr-°F) | 1.79 |
| Rock Specific Heat, Btu/(lbm-°F) | 0.202 |
| Rock Density, lbm/ft3 | 148.58 |
| Initial Water Saturation | 0.1 |
| Initial Pressure, psi | 4500 |
| Initial Temperature, °F | 238.37 |

| Fracture Properties | |
|---|---|
| Fracture Width, in | 0.24 |
| Fracture Height, ft | 160 |
| Fracture Half-Length (Injection), ft | 1000 |
| Fracture Half-Length (After Shut-in), ft | 300 |
| Fracture Conductivity (Injection), D-ft | 10 |
| Fracture Conductivity (After Shut-in), D-ft | 0.02 |
| Fracture Spacing, ft | 150 |
| Fracture Porosity | 0.2 |
| Enhanced Permeability, mD | 5.83E-03 |

| Wellbore Properties | |
|---|---|
| Wellbore Diameter, inch | 8.75 |
| Casing OD, inch | 5.5 |
| Pipe Roughness | 0.001 |
| Casing Thermal Conductivity, Btu/(ft-hr-°F) | 6.993 |
| Cement Thermal Conductivity, Btu/(ft-hr-°F) | 4.021 |

| Treatment Information | |
|---|---|
| Injection Time, min | 100 |
| Injection rate, bpm | 90 |
| Injection Fluid Temperature, °F | 80 |

4.2.1    Verification of Sandface Temperature

After the water injection, the warm-back behavior of the sandface temperature along the wellbore can be observed as shown in **Figure 4.7**. The temperature at perforated locations recovers more slowly than at the other locations after 30 days of shut-in. Non-perforated regions also have lower temperature than the geothermal temperature because they are cooled down by the injection fluid flowing in the wellbore with a high velocity. These results show that the parallel model simulates the sandface temperature considering the heat transfer between reservoir and wellbore as well as the original model does.
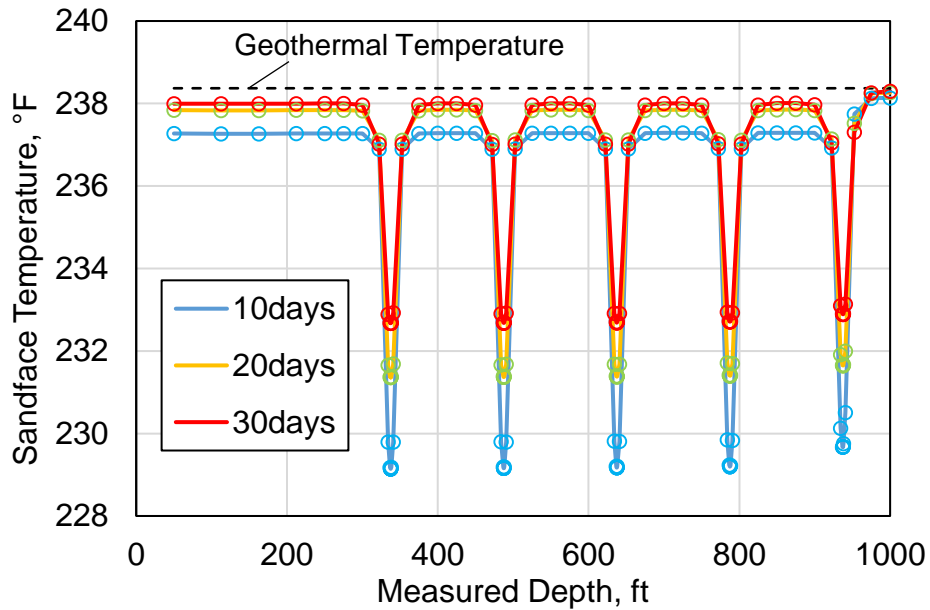


**Figure 4.7 Verification of Sandface Temperature for Five Fractures Case**

4.2.2    Verification of Wellbore Temperature

**Figure 4.8** shows the gas flow rate along the measured depth. Since the identical fractures are considered, the same production rate from each cluster is observed. During production period, the sandface temperature shows Joule-Thompson cooling effect due to the gas production, and wellbore temperature indicates the fluid mixing between the gas inflow and wellbore stream (Hill, 1990) as shown in **Figure 4.9** (b) and (c), respectively. The computation of wellbore temperature is also verified by the results.
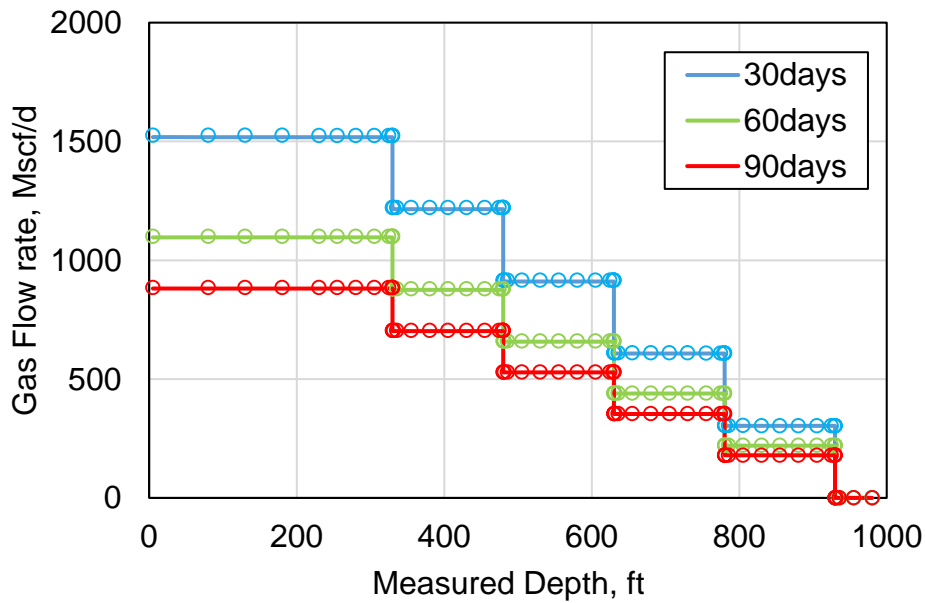


**Figure 4.8 Verification of Gas Flow rate for Five Fractures Case**
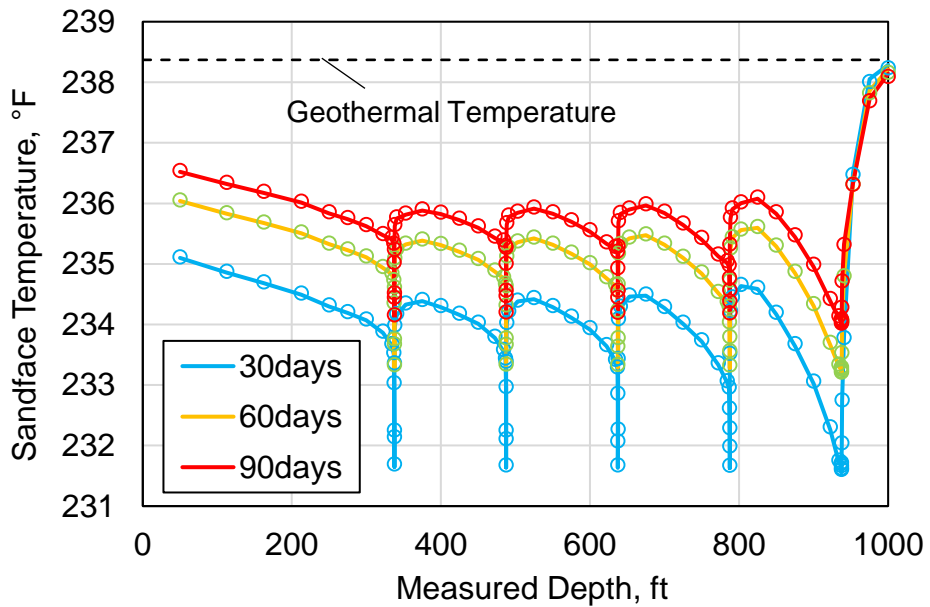
(a) Sandface Temperature
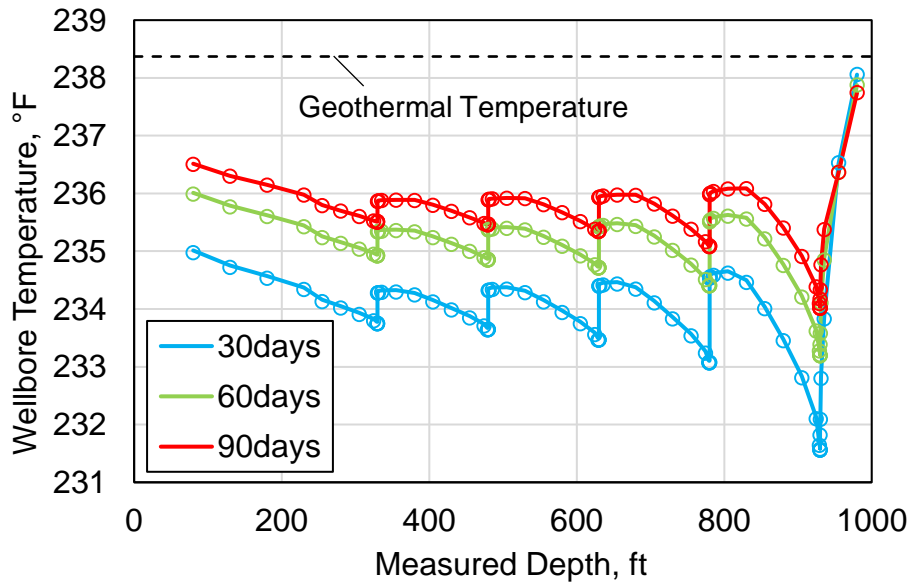

(b) Wellbore Temperature

**Figure 4.9 Verification of Temperature for Five Fractures Case**

### 4.2.3  Conclusion for Verification Study

The results provided in this chapter verify that the parallel model simulates temperature for all fracturing treatment phases correctly. Some small differences of values are observed in the results because the models are implemented by different compilers. The original model is implemented by Microsoft C#, and the parallel model is done by Intel Fortran 90/95. Those different compilers do not have the exact same decimal places. Therefore, the two simulators have small errors, but it is negligible because the differences of values are less than 0.01 %.

# CHAPTER 5

## RESULT OF COMPUTATIONAL SPEED INCREASE

5.1     Model Setup

This chapter provides the performance improvement by the parallelization in computational speed. Three different cases, a single stage, three stages, and five stages are setup as shown in **Figure 5.1** to observe the behavior of speedup by the parallelization. In the figure, the blue planes represent the treated fractures. To compare the computational time among the cases, the same properties of reservoir, fractures and wellbore are assigned as shown in **Table 5.1**. Each stage has five clusters with 50 ft of cluster spacing. The computational time for simulations of injection for one stage and production is compared in this case study.

**(a) Single Stage**

**(b) 3 Stages**

**(c) 5 Stages**
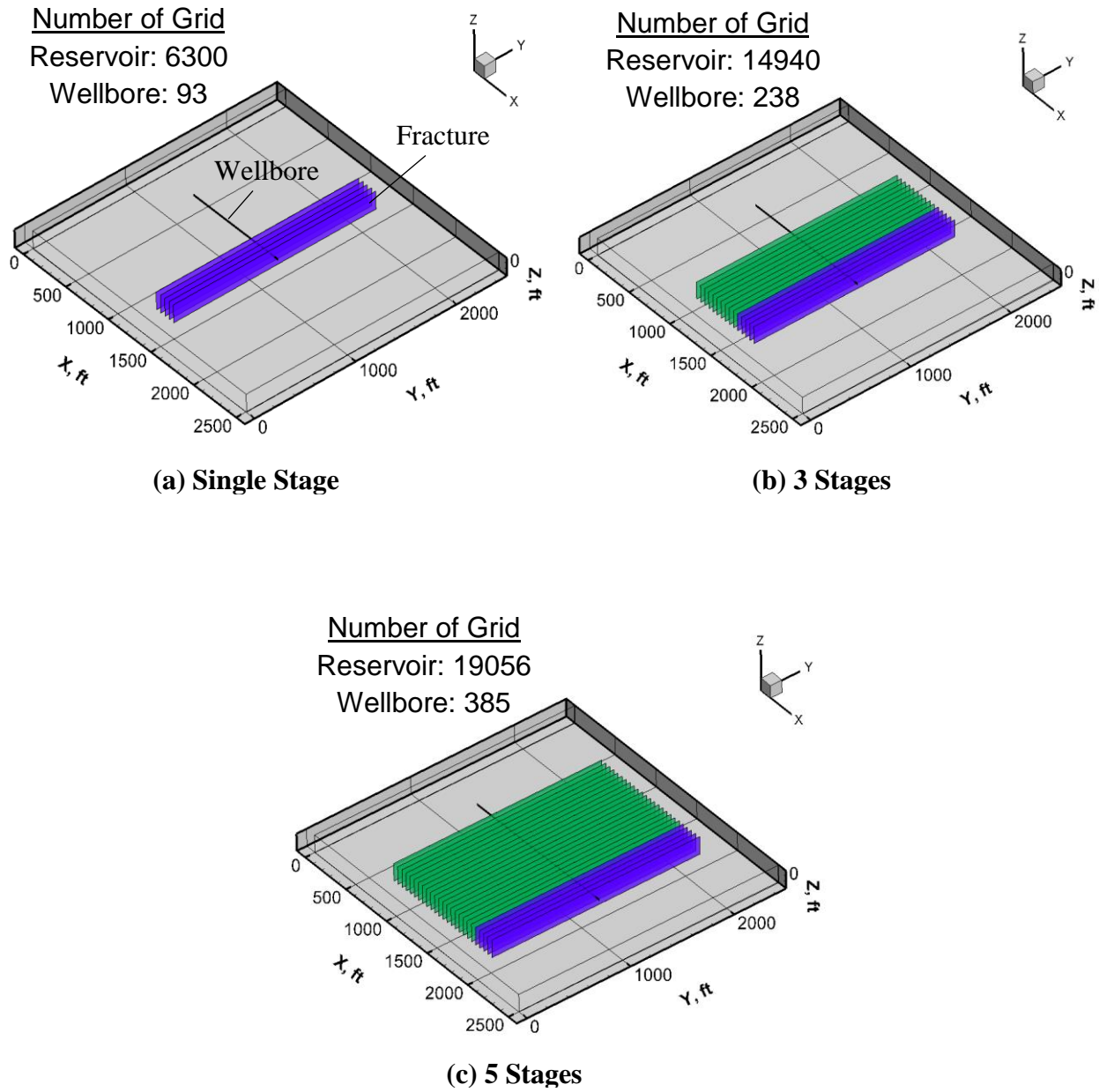
**Figure 5.1 Model Setup for Parallel Simulation Study**

**Table 5.1 Main Input Parameters for Parallel Simulation Study**

| Reservoir Properties | |
|---|---|
| Matrix Permeability, mD | 5.83E-04 |
| Matrix Porosity | 0.042 |
| Total Thermal Conductivity, Btu/(ft-hr-°F) | 1.79 |
| Rock Specific Heat, Btu/(lbm-°F) | 0.202 |
| Rock Density, lbm/ft3 | 148.58 |
| Initial Water Saturation | 0.1 |
| Initial Pressure, psi | 4500 |
| Initial Temperature, °F | 238.37 |

| Fracture Properties | |
|---|---|
| Fracture Width, in | 0.24 |
| Fracture Height, ft | 160 |
| Fracture Half-Length (Injection), ft | 1000 |
| Fracture Half-Length (After Shut-in), ft | 300 |
| Fracture Conductivity (Injection), D-ft | 10 |
| Fracture Conductivity (After Shut-in), D-ft | 0.02 |
| Fracture Porosity | 0.2 |
| Enhanced Permeability, mD | 5.83E-03 |

| Wellbore Properties | |
|---|---|
| Wellbore Diameter, inch | 8.75 |
| Casing OD, inch | 5.5 |
| Pipe Roughness | 0.001 |
| Casing Thermal Conductivity, Btu/(ft-hr-°F) | 6.993 |
| Cement Thermal Conductivity, Btu/(ft-hr-°F) | 4.021 |

| Treatment Information | |
|---|---|
| Cluster Number per Stage | 5 |
| Fracture Spacing, ft | 50 |
| Injection Time per Stage, min | 100 |
| Injection Rate per Stage, bpm | 90 |
| Injection Fluid Temperature, °F | 80 |
| Production Time, days | 100 |

5.2     Result and Discussion

5.2.1   Computational Speed Increase for Injection Cases

The three cases are simulated by the original model and the developed parallel model with different number of processors. In parallel simulation, the number of processors directly influence the computational time. **Figure 5.2** shows a comparison of computational time for each case with different number of processors in semi-log plot. The results conclude that the parallel model can simulate faster than the original model for all of the cases. They also indicate that the computational time can be improved by adjusting the number of processors in the parallel model.
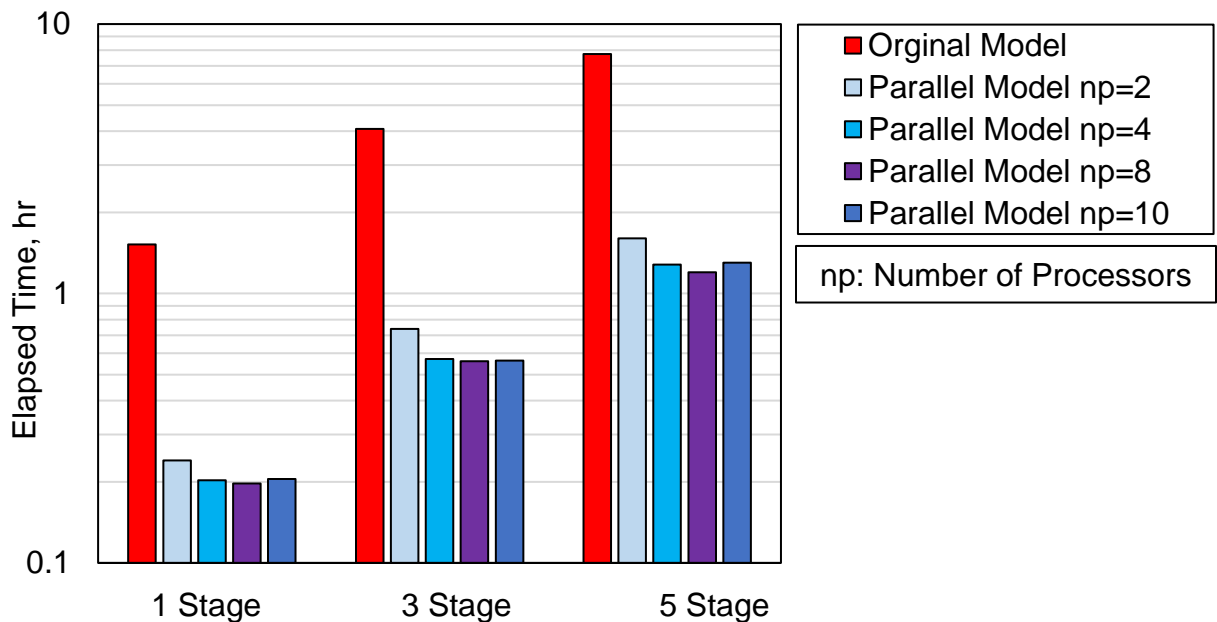


**Figure 5.2 Comparison of Computational Time for Injection Cases**

Some results by the parallel model, however, show declines in performance as the number of processors increases. To observe the behavior of speed increase, the relationship between the number of processors and the speed-up is plotted in **Figure 5.3**. The performance is improved

when the number of processors is increased from two to four, but the performance improvement stops in the case of np = 8. If the number of processors is set as np = 10, the performance declines. It is caused by the data communication among the processors. As explained in Chapter 3, the parallel model distributes data or tasks to multiple processors. Overall computations can be done by sending and receiving data among the processors. The more processors we assign, the more communications occur. Since the communications also take time, the performance declines would result. According to this study, the number of processors needs to be optimized depending on cases.



**Figure 5.3 Computational Speed Increase for Injection Cases**

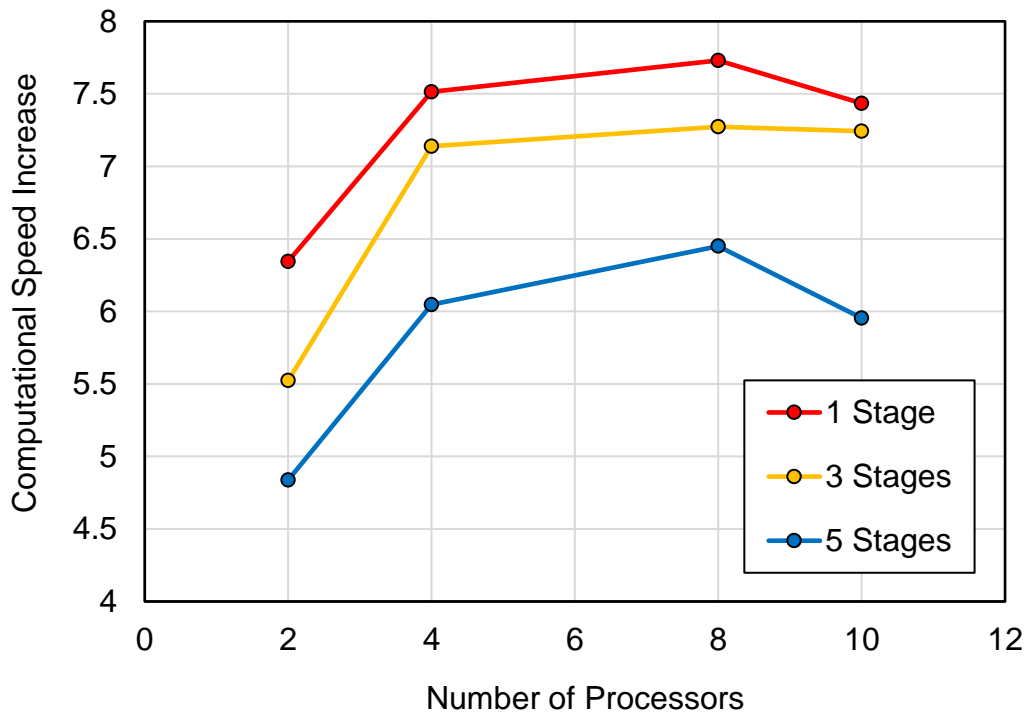Also, the number of stages or grid blocks seems to be related to the performance. The cases of multiple stages show lower performance. The possible reason is the convergence issue in the wellbore model. As explained in Chapter 3, slow convergence is observed in the wellbore model. If a large reservoir and multiple stages are set up, wellbore cells also need to be increased. Since only the reservoir model is parallelized, the number of wellbore cells would affect the convergence and the overall computational speed.

5.2.2    Computational Speed Increase for Production Cases

**Figure 5.4** shows a comparison of computational time for the simulations of production period with different number of processors in a semi-log plot. The performance improvement can be observed in the production cases as well. The production time is 100 days while the injection time is 100 minutes for one stage, but the elapsed time for the production cases is shorter than for the injection cases. The reason is the high non-linearity not only in the wellbore and also in the fractures during injection. Since the fractures are set as the grid blocks which have the infinitely high permeability, the high flow rate flowing in the fractures causes small timestep size and the long simulations for the injection cases.
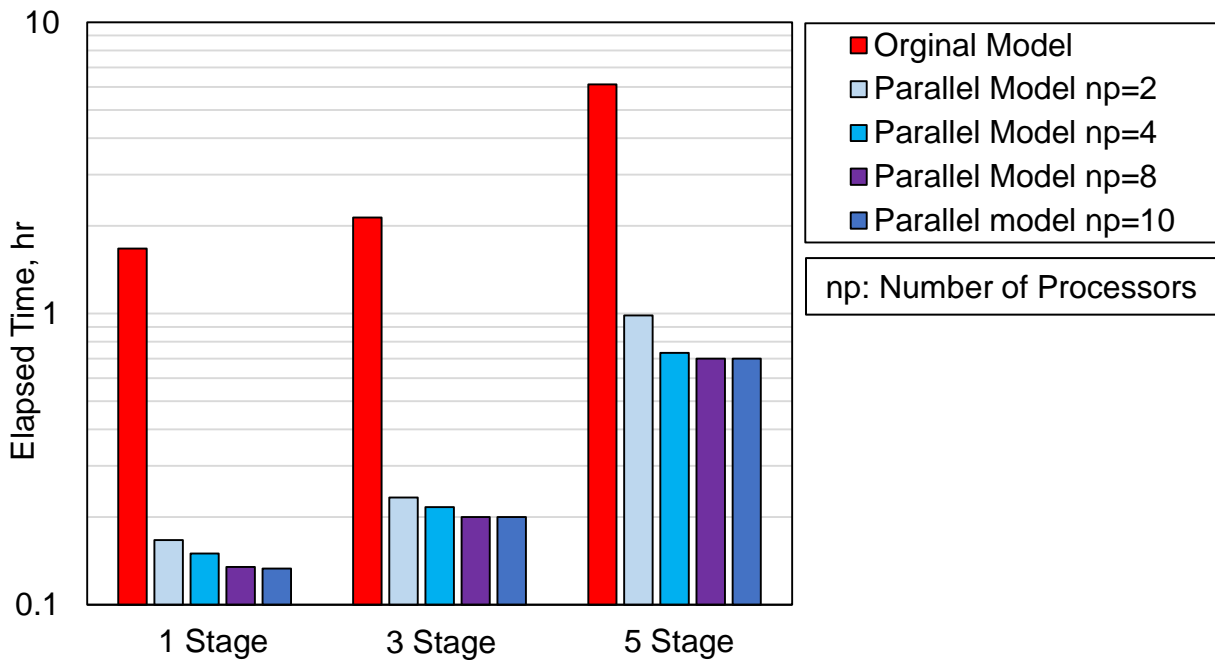
**Figure 5.4 Comparison of Computational Time for Production Cases**

**Figure 5.5** shows results of computational speed increase for both the injection and

production cases. The data communications among the processors restrict the performance for the

production cases as well. The figure indicates that the parallel model is more effective for the

production cases than for the injection cases. This seems to be produced by the convergence

behavior in the wellbore model. In production cases, the wellbore model is converged relatively

quickly. Therefore, the computational speed of the parallel reservoir model would become more

dominant in the overall simulations. However, the performance declines due to the increase of

stage number in the same way as for the injection cases. This indicates that the increase of wellbore

cells or the convergence issue in the wellbore model still affects the results of production cases.

**Figure 5.5 Computational Speed Increase for Production Cases**

CHAPTER 6

CONCLUSION AND FUTURE WORK


According to this study, we conclude that the parallel model simulates the sandface temperature in a multi-stage fractured horizontal well more efficiently than the original model does. Although this parallel model can be used as a useful tool to interpret the DTS temperature q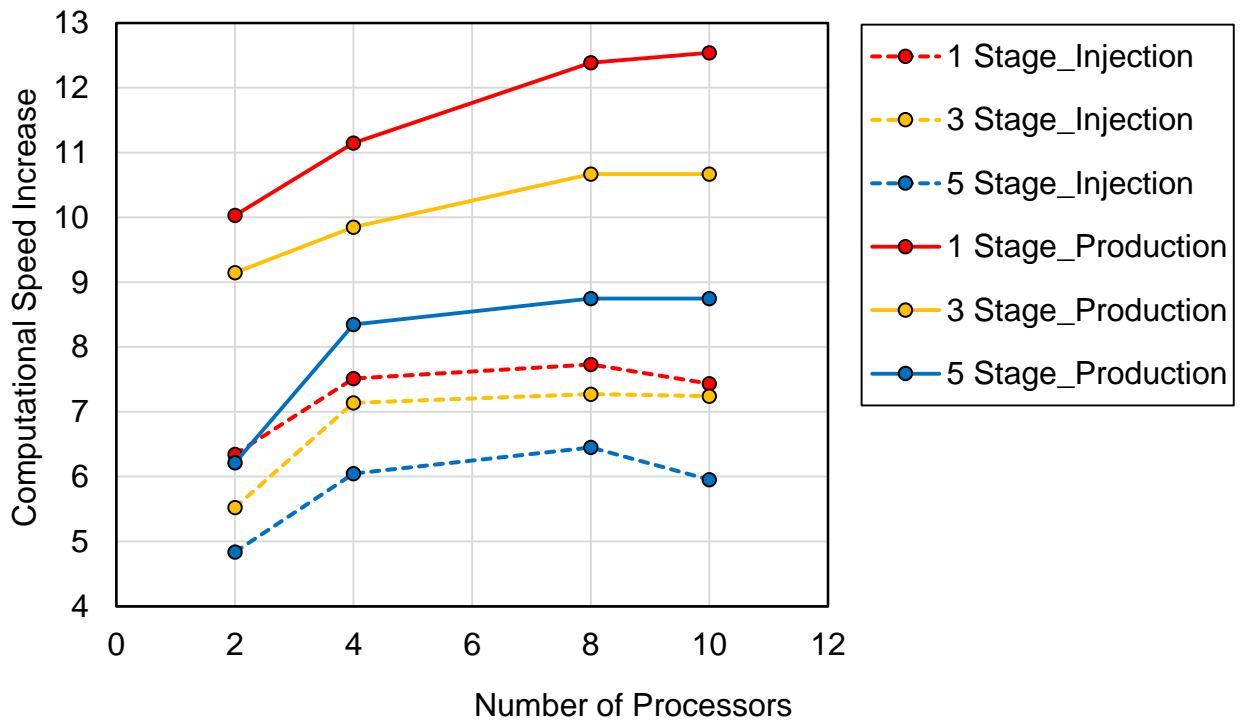uantitatively, some tasks still remain. First of all, the wellbore convergence issue as observed in the results needs to be solved to improve performance of the parallel model. According to those case studies, when a number of wellbore cells are setup, the wellbore simulation would become slow. It is expected to be solved by another solution method, for example, the semi-implicit method. Also, partition method for the parallelization should be improved. While the current parallel model separates a domain evenly, flexible separations would make the simulations faster. For instance, fine partition around the fractures is expected to provide better performance.

Besides the parallel method, the thermal and flow model needs to be improved to interpret the DTS temperature accurately. As explained in Chapter 2, the current version of the model does not simulate the DTS temperature but the sandface temperature. They may have different magnitude or behavior. To solve this problem, a different approach from the one-dimensional wellbore model is required.

# NOMENCLATURE

$A$ = cross-sectional area of a well segment, $\text{ft}^2$ $[\text{m}^2]$

$Ar$ = surface area of a well segment, $\text{ft}^2$ $[\text{m}^2]$

$C_p$ = specific heat, Btu/(lbm-°F) [J/(kg-°C)]

$f_m$ = mixture friction factor on a wall of a well segment, dimensionless

$\mathbf{g}$ = acceleration vector of gravity, $\text{ft/D}^2$ $[\text{m/s}^2]$

$\mathbf{F}^i$ = mass flux of component $i$ per unit area, $\text{lbm/(ft}^2\text{-D)}$ $[\text{kg/(m}^2\text{-s)}]$

$\mathbf{F}^\theta$ = heat flux per unit area, $\text{Btu/(ft}^2\text{-D)}$ $[\text{J/(m}^2\text{-s)}]$

$H$ = specific enthalpy, Btu/lbm [J/kg]

$h$ = heat transfer coefficient, $\text{Btu/(hr-ft}^2\text{-°F)}$ $[\text{J/(s-m}^2\text{-°C)}]$

$H^g$ = Henry's coefficient, psi [Pa]

$j$ = volumetric flux of gas-liquid mixture in wellbore, ft/D [m/s]

$j_\beta$ = superficial velocity (volumetric flux) of phase $\beta$ in wellbore, ft/D [m/s]

$k$ = intrinsic permeability, md $[\text{m}^2]$

$k_{dry}$ = dry rock thermal conductivity, $\text{Btu-ft/(hr-ft}^2\text{-°F)}$ $[\text{J-m/(s-m}^2\text{-°C)}]$

$k_f$ = fluid thermal conductivity, $\text{Btu-ft/(hr-ft}^2\text{-°F)}$ $[\text{J-m/(s-m}^2\text{-°C)}]$

$k_{wet}$ = water-saturation rock thermal conductivity, $\text{Btu-ft/(hr-ft}^2\text{-°F)}$ $[\text{J-m/(s-m}^2\text{-°C)}]$

$k_{r\beta}$ = relative permeability of phase $\beta$, dimensionless

$k_{Tt}$ = total thermal conductivity, $\text{Btu-ft/(hr-ft}^2\text{-°F)}$ $[\text{J-m/(s-m}^2\text{-°C)}]$

$M^i$ = mass accumulation of component $i$ per unit volume, $\text{lbm/ft}^3$ $[\text{kg/m}^3]$

$M^\theta$ = thermal accumulation per unit volume, $\text{Btu/ft}^3$ $[\text{J/m}^3]$

$p$ = pressure, psia [Pa]

$PI$ = productivity index

$p_G$ = partial pressure, psia [Pa]

$p^w_{sat}$ = water saturation pressure, psia [Pa]

$q_\beta$ = mass flow rate of phase $\beta$ per unit volume, lbm/(ft$^3$-D) [kg/(m$^3$-s)]

$\dot{q}_\beta$ = mass flow rate of phase $\beta$, lbm/D [kg/s]

$q^i$ = mass sink/source of component $i$ per unit volume, lbm/(ft$^3$-D) [kg/(m$^3$-s)]

$q^\theta$ = thermal sink/source per unit volume, Btu//(ft$^3$-D) [J/(m$^3$-s)]

$q_{wb}$ = conductive heat transfer rate per unit volume, Btu/(ft$^3$-D) [J/(m$^3$-s)]

$\dot{q}_{wb}$ = conductive heat transfer rate, Btu/D [J/s]

$r$ = radial direction in wellbore coordinate system , ft [m]

$r_i$ = completion inner radius (radius for wellbore flow path), ft [m]

$r_w$ = wellbore radius, ft [m]

$R$ = gas constant per mole, Btu/(mol-R) [J/(mol-K)]

$\bar{S}$ = effective saturation, dimensionless

$S_\beta$ = saturation of phase $\beta$, dimensionless

$S_{r\beta}$ = residual saturation of phase $\beta$, dimensionless

$t$ = time, D [s]

$T$ = temperature, °F [°C]

$U$ = specific internal energy, Btu/lbm [J/kg]

$U_T$ = overall heat transfer coefficient, Btu/(hr-ft$^2$-°F) [J/(s-m$^2$-°C)]

$\mathbf{v}$ = Darcy velocity (volumetric flux in reservoir), ft/D [m/s]

$v_\beta$ = in-situ phase velocity of phase $\beta$, ft/D [m/s]

$v_m$ = mean mixture velocity of center of mass, ft/D [m/s]

$w$ = fracture width, ft [m]

$x, X$ = x-directional coordinate, ft [m]

$X^i_\beta$ = mass fraction of component $i$ in phase $\beta$, dimensionless

$y, Y$ = y-directional coordinate, ft [m]

$\dot{Y}^i_\beta$ = mole fraction of component $i$ in phase $\beta$, dimensionless

$z$ = axial direction in wellbore coordinate system, ft [m]

$Z$ = compressibility factor, dimensionless


*Greek*

$\alpha$ = thermal diffusivity, ft$^2$/hr [m$^2$/s]

$y_\beta$ = hold-up of phase $\beta$, dimensionless

$\gamma$ = pipe open ratio, dimensionless

$\Gamma$ = perimeter of a well segment, ft [m]

$\theta$ = radial direction in wellbore coordinate system, radian

$\mu$ = viscosity, cP [Pa-s]

$\rho$ = density, lbm/ft$^3$ [kg/m$^3$]

$\phi$ = porosity, dimensionless

$\varphi$ = well inclination to horizontal line, radian


*Superscripts and Subscripts*

*ann* = annulus

$\beta$ = phase

$c$ = casing

59

$cem$ = cement

$f$ = fluid

$fr$ = fracture

$I$ = inflow

$IG$ = ideal gas

$i$ = component

$l$ = liquid

$r$ = rock

$s$ = solid

$t$ = tubing

REFERENCE

Class, H., Helmig, R. and Bastian, P. 2002. *Numerical Simulation of Non-Isothermal Multiphase Multicomponent Processors in Porous Media.*: 1. An efficient Solution Technique. *Advances in Water Resources* **25** (5): 533-550. doi: 10.1016/S0309-1708(02)00014-3.

Coats, K.H. 1977. Geothermal Reservoir Modelling. Presented at the SPE Annual Fall Technical Conference and Exhibition, Denver, Colorado, USA, 9-12 October. SPE-6892-MS. doi: 10.2118/6892-MS.

Corey, A.T. 1954. The Interrelation Between Gas and Oil Relative Permeabilities. *Producers Monthly* **19** (November): 38-41.

Cui, J., Zhu, D. and Jin, M. 2015. Diagnosis of Production Performance after Multistage Fracture Stimulation in Horizontal Wells by Downhole Temperature Measurements. SPE Production & Operations Preprint. SPE-170874-PA. doi: 10.2118/170874-PA.

Davis, E.R., Zhu, D. and Hill, A.D. 1997. Interpretation of Fracture Height from Temperature Logs - The Effect of Wellbore/Fracture Separation. SPE Formation Evaluation 12 (02): 119-124. SPE-29588-PA. doi: 10.2118/29588-PA.

Gropp, W., Lusk E., Thakur, R. 1999. *Using MPI-2*, Massachusetts Institute of Technology. 11-50.

Hill, A.D. 1990. *Production Logging: Theoretical and Interpretive Elements*, Henry L. Doherty Memorial Fund of AIME, Society of Petroleum Engineers, Richardson, Texas. 19-36.

Huber, M.L., Perkins, R.A., Laesecke, A. et al. 2009. New International Formulation for the Viscosity of H2O. *Journal of Physical and Chemical Reference Data* **38** (2): 101-125. doi: 10.1063/1.3088050.

Ishii, M. 1977. One-Dimensional Drift-Flux Model and Constitutive Equations for Relative Motion Between Phases in Various Two-Phase Flow Regimes. Technical Report ANL-77-47, DOE Contract No. W-31-109-ENG-38, Argonne National Laboratory, Argonne, Illinois (01 October 1977). doi: 10.2172/6871478.

Peaceman, D.W. 1978. Interpretation of Well-Block Pressures in Numerical Reservoir Simulation (Includes Associated Paper 6988). *Society of Petroleum Engineers Journal* **18** (3): 183-194. SPE-6893-PA. doi: 10.2118/6893-PA.

Peaceman, D.W. 1983. Interpretation of Well-Block Pressures in Numerical Reservoir Simulation with Nonsquare Grid Blocks and Anisotropic Permeability. *Society of Petroleum Engineers Journal* **23** (3): 531-543. SPE-10528-PA. doi: 10.2118/10528-PA.

Peng, D.-Y. and Robinson, D.B. 1976. A New Two-Constant Equation of State. *Industrial and Engineering Chemistry: Fundamentals* **15** (1): 59-64. doi: 10.1021/i160057a011.

Pruess, K., Oldenburg, C. and Moridis, G. 1999. *TOUGH2 User's Guide*, Version 2.0. Lawrence Berkeley National Laboratory, Berkeley, California.

Ramey, H.J. 1962. Wellbore Heat Transmission. *Journal of Petroleum Technology* 14 (4): 427-435. SPE-96-PA. doi: 10.2118/96-PA.

Seth, G., Reynolds, A.C. and Mahadevan, J. 2010. Numerical Model for Interpretation of Distributed-Temperature-Sensor Data During Hydraulic Fracturing. Presented at the SPE Annual Technical Conference and Exhibition, Florence, Italy, 19-22 September. SPE-135603-MS. doi: 10.2118/135603-MS.

Sierra, J.R., Kaura, J.D., Gualtieri, D., Glasbergen, G., Sarkar, D. and Johnson, D. 2008. DTS Monitoring Data of Hydraulic Fracturing: Experiences and Lessons Learned. Presented at the SPE Annual Technical Conference and Exhibition, Denver, Colorado, USA, 21-24 September. SPE-116182-MS. doi: 10.2118/116182-MS.

Somerton, W.H., El-Shaarani, A.H. and Mobarak, S.M. 1974. High Temperature Behavior of Rocks Associated with Geothermal Type Reservoirs. Presented at the SPE California Regional Meeting, San Francisco, California, USA, 4-5 April. SPE-4897-MS. doi: 10.2118/4897-MS.

Tabatabaei, M. and Zhu, D. 2012. Fracture-Stimulation Diagnostics in Horizontal Wells through Use of Distributed-Temperature-Sensing Technology. SPE Production & Operations 27 (4): 356-362. SPE-148835-PA. doi: 10.2118/148835-PA.

Ugueto, G.A., Huckabee, P.T. and Molenaar, M.M. 2015. Challenging Assumptions about Fracture Stimulation Placement Effectiveness Using Fiber Optic Distributed Sensing Diagnostics: Diversion, Stage Isolation and Overflushing. Presented at the SPE Hydraulic Fracturing Technology Conference, The Woodlands, Texas, USA, 3-5 February. SPE-173348-MS. doi: 10.2118/173348-MS. 138

Ugueto, G.A., Huckabee, P.T., Molenaar, M.M., Wyker, B. and Somanchi, K. 2016. Perforation Cluster Efficiency of Cemented Plug and Perf Limited Entry Completions; Insights from Fiber Optics Diagnostics. Presented at the SPE Hydraulic Fracturing Technology Conference, The Woodlands, Texas, USA, 9-11 February. SPE-179124-MS. doi: 10.2118/179124-MS.

Wagner, W., Cooper, J.R., Dittmann, A., Kijima, J., Kretzschmar, H.J., Kruse, A., Mareš, R., Oguchi, K., Sato, H., Stöcker, I., Šifner, O., Takaishi, Y., Tanishita, I., Trübenbach, J. and Willkommen, T. 2000. The IAPWS Industrial Formulation 1997 for the Thermodynamic Properties of Water and Steam. *Journal of Engineering for Gas Turbines and Power* **122** (1): 150-184. doi: 10.1115/1.483186.

Yoshida, N., Zhu, D. and Hill, A.D. 2014. Temperature-Prediction Model for a Horizontal Well With Multiple Fractures in a Shale Reservoir. SPE Production & Operations 29 (4): 261-273. SPE-166241-PA. doi: 10.2118/166241-PA.

Yoshida, N. 2016. Modeling and Interpretation of Downhole Temperature in a Horizontal Well with Multiple Fractures. Ph.D. dissertation, Texas A&M University.

Yoshida, N., & Hill, A.D. 2016. Comprehensive Modeling of Downhole Temperature in a Horizontal Well with Multiple Fractures. Society of Petroleum Engineers. SPE-181812. doi:10.2118/181812-MS

Yoshioka, K. 2007. Detection of Water or Gas Entry into Horizontal Wells by Using Permanent Downhole Monitoring Systems. PhD Dissertation, Texas A&M University, College Station, Texas (May 2007). 139

Yoshioka, K., Zhu, D., Hill, A.D., Dawkrajai, P. and Lake, L.W. 2005. A Comprehensive Model of Temperature Behavior in a Horizontal Well. Presented at the SPE Annual Technical Conference and Exhibition, Dallas, Texas, USA, 9-12 October. SPE-95656-MS. doi: 10.2118/95656-MS.

Yoshioka, K., Zhu, D., Hill, A.D., Dawkrajai, P. and Lake, L.W. 2007. Prediction of Temperature Changes Caused by Water or Gas Entry into a Horizontal Well. SPE Production & Operations 22 (4): 425-433. SPE-100209-PA. doi: 10.2118/100209-PA.

Yoshioka, K., Zhu, D., Hill, A.D. and Lake, L.W. 2009. A New Inversion Method to Interpret Flow Profiles from Distributed Temperature and Pressure Measurements in Horizontal Wells. SPE Production & Operations 24 (4): 510-521. SPE-109749-PA. doi: 10.2118/109749-PA.

Yaws, C.L. 1995. *Handbook of Transport Property Data: Viscosity, Thermal Conductivity, and Diffusion Coefficients of Liquids and Gases*, Gulf Pub. Co., Houston Texas.

Yaws, C.L. 2008. *Thermophysical Properties of Chemicals and Hydrocarbons*, Elsevier Science BV, Amsterdam.